Research Square

Preprints are preliminary reports that have not undergone peer review.
They should not be considered conclusive, used to inform clinical practice,
or referenced by the media as validated information.

NIR-Activated NO-Propelled Nanomotors for Deep Tumor Penetration and DNA-Repair Sensitized Photothermal Therapy of Prostate Cancer

Jie He
Guizhou University
Xiaoli Zhang
Guizhou University
Qiqi Yang
Guizhou Medical University
Ji Sun
Guizhou Medical University
Yu An
Guizhou Provincial People's Hospital
Kehua Jiang
Guizhou Provincial People's Hospital
Fa Sun
Guizhou University
Janguo Zhu
Guizhou University
Kun Chen
44844956@qq.com

Guizhou Provincial People's Hospital

Research Article

Keywords: Controlled release, Nitric oxide, BLM helicase inhibition, Deep penetration, Prostate cancer

Posted Date: March 17th, 2026

DOI: https://doi.org/10.21203/rs.3.rs-9091462/v1

License: This work is licensed under a Creative Commons Attribution 4.0 International License.
Read Full License

Additional Declarations: No competing interests reported.

Version of Record: A version of this preprint was published at Journal of Nanobiotechnology on August 11th, 2026. See the published version at https://doi.org/10.1186/s12951-026-04886-1.

NIR-Activated NO-Propelled Nanomotors for Deep Tumor Penetration and DNA-Repair Sensitized Photothermal Therapy of Prostate Cancer

Jie He[a,c,1], Xiaoli Zhang[a,1], Qiqi Yang[e], Ji Sun[e], Yu An[c,d], Kehua Jiang[f], Fa Sun[a,*], Janguo Zhu[a,f,*], and Kun Chen[b,*]

[a] *Medical College, Guizhou University, Guizhou 550000, P. R. China*

[b] *Department of Medical Genetics, Guizhou Provincial People's Hospital, Guizhou 550000, P. R. China*

[c] *Central Laboratory, Guizhou Provincial People's Hospital, Guizhou 550000, P. R. China*

[d] *NHC Key Laboratory of Pulmonary Immune-related Diseases, Guizhou Provincial People's Hospital, Guizhou 550000, P. R. China*

[e] *Guizhou Medical University, Guizhou 550000, P. R. China*

[f] *Department of Urology, Guizhou Provincial People's Hospital, Guizhou 550000, P. R. China*

[1] These authors contributed equally to this work.

* Corresponding author. Guizhou Provincial People's Hospital, No. 83, Zhongshan East Road, Guiyang, Guizhou, 550002, P.R. China. Phone: 86-0851-85937212

E-mail Address: 44844956@qq.com (K. Chen); sfgmc@sina.com (F. Sun); doctorzhujianguo@163.com (J. Zhu).

Abstract: Photothermal therapy (PTT) for solid prostate cancer (PCa) is often limited by poor intratumoral penetration and rapid DNA repair. Herein, we engineered a PSMA-targeted gas nanomotor that couple deep tumor penetration with DNA repair sensitization for enhanced photothermal/NO therapy. BLM helicase inhibitor ML216 and nitric oxide donor BNN6 were co-encapsulated with phase-change material and loaded into single-pore hollow polydopamine nanoparticles, followed by surface conjugation with anti-PSMA nanobodies (VHH) to yield M/B@PDA-VHH NPs. VHH-mediated recognition confers active targeting toward PSMA-positive PCa cells. Under near-infrared irradiation, the nanoparticles show high photothermal conversion and trigger on-demand release of NO and ML216. NO generation propels nanomotor movement, markedly improving transport across endothelial barriers, penetration into 3D tumor spheroids, and distribution in PCa tissues in vivo. Photothermal/NO treatment induces DNA damage and promote apoptosis. Released ML216 inhibits BLM helicase, leading to replication fork stalling and accumulation of double-strand breaks, and concomitantly suppresses AKT/mTOR signaling via dephosphorylation of p-AKT and p-PRAS40. These effects disrupt DNA repair and amplify oxidative damage, restoring therapeutic sensitivity. In vitro and in vivo studies show strong tumor growth inhibition with minimal systemic toxicity. This gas-propelled platform offers a strategy to overcome stromal barriers and resistance in solid PCa.

Keywords: Controlled release, Nitric oxide, BLM helicase inhibition, Deep penetration, Prostate cancer

1. Introduction

Prostate cancer (PCa) remains one of the most frequently diagnosed malignancies in men [1]. In many undeveloped regions, considerable proportion of patients are diagnosed at advanced stages, resulting in poorer prognoses and limited therapeutic efficacy [2]. Current treatment modalities for advanced and castration-resistant PCa encompass androgen deprivation therapy, chemotherapy, radiotherapy, and poly (ADP-ribose) polymerase inhibitors [3]. Nevertheless, these strategies are frequently hampered by systemic toxicity, acquired drug resistance, and inadequate drug penetration into tumor tissues [4]. Consequently, there remains an urgent and unmet need for innovative therapeutic platforms that can enhance tumor-specific delivery, overcome stromal barriers, and simultaneously target multiple resistance pathways.

Nanotechnology has emerged as a transformative approach for cancer therapy, enabling targeted drug delivery, enhanced bioavailability, and multifunctional treatment modalities. Among these, nanomaterials based photothermal therapy (PTT) has gained considerable attention due to its spatiotemporal controllability, minimal invasiveness, and capacity to synergize with other treatment modalities [5]. By converting near-infrared (NIR) light into localized heat, PTT can directly ablate tumor cells and trigger the release of therapeutic agents from nanocarriers. However, conventional high-temperature PTT often requires temperatures exceeding 50 °C to achieve complete tumor eradication, which can cause unintended damage to surrounding healthy tissues, trigger inflammatory responses, and upregulate heat shock proteins that contribute to PTT resistance [6]. In contrast, mild PTT (< 50 °C) presents a safer profile but may be insufficient as a standalone treatment, necessitating combination with other therapeutic approaches to enhance its efficacy.

Nitric oxide (NO) gas therapy has recently gained considerable attention as a potent complement to photothermal treatment. As a diffusible molecule, NO can penetrate deeply into

tumor tissue, bypassing many biological barriers that limit conventional drug delivery [7]. At elevated concentrations, NO exerts multifaceted anticancer effects, including induction of DNA damage, inhibition of mitochondrial respiration, and promotion of apoptotic pathways [8]. To achieve adequate local concentrations of NO, Stimuli-responsive nano-delivery system have been engineered to facilitate NO release while minimizing premature leakage before reaching the tumor site, thereby mitigating systemic toxicity.Except for endogenous triggers present in the tumor microenvironment—such as acidity, elevated glutathione, and high esterase activity—light-responsive platforms offer distinct advantages by enabling non-invasive and spatially controlled NO release [9].

Despite this promising synergy, the effective delivery of both photothermal agents and NO donors to deep tumor regions remains a formidable obstacle. Solid tumors are marked by dense stromal networks, high interstitial fluid pressure, and heterogeneous vascularization, which collectively impede nanoparticles (NPs) penetration and lead to heterogeneous treatment outcomes. To address this limitation, self-propelled nanomotors have been introduced as an innovative delivery platform capable of actively navigating through biological matrices. These nanoscale systems can convert external energy (e.g., light, ultrasound) or endogenous chemical fuels (e.g., glucose, urea) into mechanical motion, thereby enhancing their diffusion and tissue penetration [10]. In particular, NO-propelled nanomotors present a distinctive therapeutic advantage by fulfilling a dual role of cytotoxic agent and propulsion source. Upon NIR irradiation, such nanomotors can release NO in a controlled manner, generating thrust forces that enhance their mobility and tissue penetration, while simultaneously delivering cytotoxic NO to cancer cells [11]. This dual functionality establishes a self-reinforcing cycle wherein the release of NO gas facilitates NPs movement, thereby promoting deeper tissue penetration and more homogeneous distribution.

Beyond physical barriers, PCa cells often deploy robust DNA repair mechanisms and pro-survival signaling pathways that confer resistance to conventional DNA-damaging therapies [12] including those PTT/NO based therapy. The Bloom syndrome helicase (BLM) plays a pivotal role in homologous recombination repair and replication fork stabilization. Overexpression of BLM has been associated with PCa progression and therapeutic resistance [13]. ML216 is a typical pharmacological inhibition of BLM helicase, which sensitize cancer cells to DNA-damaging agents by impairing repair capacity and disrupting survival cascades such as the AKT/mTOR pathway [14]. To the best of our knowledge, leveraging DNA-repair inhibition to potentiate NO/PTT therapy in PCa remains underexplored.

Inspired by these advances, we designed the multifunctional nanoplatform that merges deep-tumor penetration with DNA repair inhibition for precise PCa therapy. The BLM helicase inhibitor ML216 and the NO donor N, N'-dinitroso-1,4-phenylenediamine (BNN6) were co-encapsulated within a temperature-responsive phase-change material (PCM) and loaded into single-pore hollow polydopamine (PDA) NPs, followed by surface conjugation with anti-prostate cancer membrane antigen (anti-PSMA) nanobodies (VHH) to construct M/B@PDA-VHH NPs (Scheme 1a). The VHH moiety enables active targeting to PSMA-positive PCa cells. Under NIR irradiation, the PDA shell generates localized heat, which melts the PCM and triggers the controlled release of both NO and ML216. The released NO not only propels the NPs, enhancing their penetration across tumor tissues, but also synergizes with PTT to induce oxidative stress and DNA damage. Concurrently, ML216 inhibits BLM helicase activity, leading to replication fork arrest, accumulation of double-strand breaks, and suppression of the AKT/mTOR survival pathway via dephosphorylation of AKT and PRAS40 (scheme 1b). Collectively, the combination of PTT/NO-based DNA damage amplification and ML216-mediated blockade of pro-survival signaling offers a comprehensive strategy for enhanced PCa treatment.

2. Experimental section

2.1. Materials

Dopamine hydrochloride, lauric acid, stearic acid, ethyldimethylaminopropyl carbodiimide (EDC), N-hydroxysuccinimide (NHS), N, N-Di-sec-butyl-N, BNN6, ML216, Rhodamine B,dihydrochloride, TritonX-100, trypsin,4',6-Diamidino-2-phenylindole (DAPI), 2',7'-Dichlorodihydrofluorescein diacetate (DCFH-DA) and 4-Amino-5-methylamino-2',7'-difluorofluorescein diacetate (DAF-FM DA) were acquired from Sigma-Aldrich (St. Louis, USA). NO test kit, apoptosis detection kit，Cell Counting Kit-8 (CCK-8), mitochondrial membrane potential detection kit and Calcein-AM/PI were purchased from the Biyotime Biotechnology Co., Ltd (Shanghai China). The PCa cell lines 22RV1 and PC-3, along with human umbilical vein endothelial cells (HUVECs), NIH3T3 and normal prostate epithelial cells (RWPE-1) were obtained from the American Type Culture Collection (Manassas, USA). Polystyrene (PS) nanospheres (200 nm) were obtained from Yiyuan Biotechnology Co., Ltd (Shanghai, China). Rabbit anti-rabbit antibodies of AKT, Phosphorylated AKT (p-AKT,Ser473)， PRAS40，Phosphorylated PRAS40(p-PRAS40,Thr246)， caspase-3, Ki-67 and goat anti-rabbit IgG-horseradish peroxidase developer were purchased from Abcam Shanghai Trading Co., Ltd (Shanghai, China). All the chemicals were supplied by Adamas-beta unless otherwise noted.

2.2. Synthesis of hollow PDA(HPDA) NPs

Scheme 1a illustrates the preparation of HPDA NPs through creating PDA coated PS (PS@PDA) NPs and etching PS cores. Briefly, 0.5 mL of 2.5% (w/v) PS nanosphere suspension was mixed with 10 mL of Tris-HCl buffer (pH 8.5), followed by the addition of 10 mL of dopamine hydrochloride (1 mg/mL). The resulting mixture was then kept at ambient temperature for 12 or

24 h. The collected PS@PDA (10 mg) core-shell NPs were dispersed in 10 mL of sodium dodecyl sulfate/toluene/water (m/v/v,0.1/0.1/.9.9) solutions, followed by incubation at 25℃ for 6 h. The etching process was quenched by adding 20 mL ethanol, and the collected precipitate was resuspended with 10 mL tetrahydrofuran for 4 h to ensure complete etching of the PS core to obtain HPDA NPs [15].

2.3. Preparation of M/B@PDA-VHH NPs

The PCM penetrated into HPDA NPs through surface nanopores, enabling controlled drug encapsulation via this structural permeability [16]. Briefly, the 0.5 g of lauric acid/stearic acid mixture (m/m, 4/1) was heated until completely melted and then homogenized thoroughly with 0.5 mL of a dimethyl sulfoxide solution containing 40 mg of ML216 and 40 mg of BNN6. Afterwords, 5 mg of HPDA NPs were added, following stirring at 300 rpm for 2 h, the drug-loaded PCM was allowed to permeate the HPDA nanostructure. The obtained precipitate was collected and incubation with deionized water to solidify the PCM, and washed with dimethyl sulfoxide solution to remove unloaded drugs. The purified M/B@PDA product was stored at 4 °C for subsequent assays. For comparison, control NPs loaded solely with ML216 (M@PDA) or BNN6 (B@PDA) were prepared following the same procedure by addition of alone drug component.

The targeting capacity of three antibodies (VHH2, VHH3, and VHH4) are screened in terms of PSMA-positive PCa cells (22RV1)，using PSMA-negative (PC-3)cells as controls [17]. Briefly, the FITC-labeled nanobodies VHH2, VHH3 and VHH4 were co-incubated with PSMA-positive PCa cells 22RV1 at 37 °C with 12 h. Subsequently, the fluorescent signal intensity of FITC was detected by flow cytometry (FCM, BD FACSCelesta™，USA)to evaluate the targeting effect of VHH. The selected VHH3 were conjugated to the surface of M/B@PDA NPs by amination

reaction. Briefly, VHH3 (0.2 mg/mL, 20 μL), EDC (5.0 mg/mL, 20 μL), NHS (5.0 mg/mL, 10 μL) were stirred in PBS for 4 h to activate the carboxyl group, followed by adding M/B@PDA (5.0 mg) and reacting at 37 °C for 12 h. The resulting M/B@PDA-VHH were isolated by centrifugation [18]. The grafting efficiency of VHH3 onto M/B@PDA NPs was determined by quantifying the unbound VHH3 remaining in the supernatant relative to the initial amount added [19].

2.4. Characterization of M/B@PDA-VHH NPs

The hollow structure of the NPs was confirmed using transmission electron microscope (TEM, JEM-F200, Japan).Scanning electron microscopy (SEM, Zeiss Gemini SEM 300, Germany) was employed to characterize the surface morphology. The average particle size and zeta potential of the NPs were determined using dynamic light scattering (DLS, Malvern Nano-ZS90, UK). The elemental composition of the NPs surface was characterized by XPS (Thermo Scientific K-Alpha, USA). And the modification of VHH3 were evaluated on sodium dodecyl sulfate-polyacrylamide gel electrophoresis (SDS-PAGE). The loading rate of BNN6 and ML216 were determined by high-performance liquid chromatography system (HPLC, Agilent 1260 Infinity, Germany) according to the added amounts [20]. The long-term stability of M/B@PDA-VHH NPs was investigated by DLS analysis.

2.5. Photothermal properties of M/B@PDA-VHH NPs

To investigate the photothermal behavior, 0-300 μg/mL M/B@PDA-VHH NPs were exposed to 808 nm NIR (0.5-2.5 W/cm^2, KS-810F-8000, China) for 5 min. Thermal images were recorded every 60 s to monitor the suspension temperature by using an infrared camera (Fluke Ti480, USA). For photothermal stability assessment, M/B@PDA-VHH NPs underwent four NIR irradiation ON/OFF cycles with natural cooling to environment temperature between cycles [21]. Subsequent calculation of the photothermal conversion efficiency (η) was performed using established

methods [22].

$$\eta = \frac{hS\ \ (S_{max}\text{-}T_{suur}) - Q_{Dis}}{I(1-10^{-A808})}$$

where T_{max} is the maximum temperature of the M/B@PDA-VHH suspensions, T_{surr} refer to the ambient temperature, A_{808} is the absorbance of the M/B@PDA-VHH solution at 808 nm, Q_{Dis} denotes the heat dissipated from laser energy absorbed through the cuvette, while I corresponds to the incident laser power.And the hS is calculated using the following equation:

$$hS = \frac{C_D m_D}{\tau_s}$$

where C_D=4.2 J/g, m=0.3 g, and τ_s is the slope of the line obtained by fitting the cooling time t to -ln θ:

$$\theta = \frac{T\text{-}T_{suur}}{T_{max}\text{-}T_{suur}}$$

2.6. The ML216 and NO release from M/B@PDA-VHH NPs

The release profiles of ML216 and NO from the NPs were assessed in PBS under conditions with or without NIR irradiation. Briefly, M/B@PDA-VHH (5 mg) NPs were dispersed in dialysis bag (3.5 kDa) and subsequently incubated in PBS (10 mL, pH 7.4). At designated time points, the sample was subjected to irradiation with NIR, followed by a 5 min interval without irradiation. This laser on/off cycle was repeated twice. Subsequently, 1 mL of the release medium was collected for ML216 and NO detection. The concentration of ML216 was determined immediately by HPLC. NO generation was quantified in real time using the Griess agents [23].

2.7. Motion and penetration assay of M/B@PDA-VHH NPs

The motion profiles of B/M@PDA-VHH NPs were investigated in PBS containing 3 mg/mL of hyaluronic acid to simulate tumor microenvironment [24], and motion trajectories were recorded

using Dark-field optical microscopy (Olympus BX43, Japan) with a charge-coupled device camera at 25 fps under NIR irradiation. According to established protocols [25], motion trajectories were analyzed and processed using ImageJ and MATLAB to calculate the velocity and mean square displacement (MSD) of the NPs.

The penetration capacity of M/B@PDA-VHH NPs was evaluated using a typical transwell assay, which partially mimicking cell layer intercellular interactions observed in biological tissues [26]. Briefly, 10 mg of NPs were suspended in 20 mL of deionized water under ultrasound condition, followed by adding EDC (4.0 mg, 1.04 mM) and NHS (6.0 mg, 2.61 mM) to activate carboxy group for 2 h, and then reacted with rhodamine B (10.0 mg, 1.04 mM) for 12 h. The rhodamine B-labeled NPs were centrifuged, washed with deionized water to remove free rhodamine B, and then dried under vacuum. Transwell chamber (0.4 μm, Corning) was employed to evaluate the vascular-to-tumor penetration ability of the NPs. HUVECs (1×104 cells/mL)were seeded in the upper chambers to simulate the vascular endothelial barrier, while 22RV1 cells were cultured in the lower chamber. Rhodamine B labeled M/B@PDA-VHH were added into upper chambers and incubated for 6 h. Samples were exposed to NIR irradiation for 5 min. Cells in the lower chamber were fixed and nuclei were stained with Hoechst 33342 (5 μg/mL). Cellular localization of NPs was visualized by confocal laser scanning microscope (Zeiss CLSM 980, Germany). Fluorescence images were acquired and quantitatively analyzed with ImageJ software.

In the three-dimensional(3D) culture environment, the formed spheroids reflect the forces between Z-axis cells and the osmotic gradient of various substances, thus improving the accuracy of cell experiments in vitro [27]. 22RV1 and NIH3T3 cells were mixed at a 1:1 ratio (5×10^3 cells/well) and seeded into a 96-well with ultra-low attachment round-bottom plate. The plate was sealed with parafilm and centrifuged using a microplate centrifuge under controlled conditions (4 °C, 1000 g, 10 min) to facilitate three-dimensional multicellular tumor spheres formation, and

incubation with rhodamine B labeled M/B@PDA-VHH NPs for 6 h. Samples were subjected to continuous NIR exposure for 5 min, and observed using CLSM with Z-axis stack imaging.

2.8. The PCa-targeting properties of the M/B@PDA-VHH NPs in vitro

The 22RV1 cells (1×10^4cells/well) were allowed to adhere overnight. The cells were subsequently treated with rhodamine B labeled M/B@PDA-VHH NPs for 0, 2, 4, 6,8 and 12 h. then lysed by Triton X-100 (5%) at 4°C for 2 h. Intracellular rhodamine B levels were quantified using fluorescence spectrophotometry (excitation/emission: 480/590 nm) to assess NPs uptake efficiency. Parallel experiments were conducted for FCM analysis of NPs internalization under identical treatment conditions. Following fixation in 4% paraformaldehyde, the 22RV1 cells were incubated with Hoechst 33342 (5 μg/mL) and imaged by CLSM. To evaluate the targeted inhibitory effect of PSMA protein on NPs. Rhodamine B-labeled M/B@PDA and M/B@PDA-VHH NPs were co-incubated with 22RV1 cells before and after co-incubation with PSMA protein, and the targeted inhibitory performance of the active sites that masked VHH on 22RV1 cells was evaluated and analysis by CLSM.

2.9. Anti-PCa efficacy of M/B@PDA-VHH NPs in vitro

Intracellular ROS and NO levels were assessed using DCFH-DA and DAF-FM DA probes, respectively. 22RV1 cells were exposed to M/B@PDA-VHH NPs for 4 h, using M/B@PDA, M@PDA-VHH, B@PDA-VHH, and PBS as controls. After washing with PBS, cells were treated with 10 μM DCFH-DA or DAF-FM DA. Subsequently, cells were irradiated with NIR laser for 5 min, counterstained with Hoechst 33342, and imaged by CLSM.

The cytotoxic effects of M/B@PDA-VHH NPs were evaluated via Calcein-AM/PI live/dead staining and Annexin V-FITC/7-AAD apoptosis assay. 22RV1 cells were treated with M/B@PDA-

VHH NPs for 6 h, followed by NIR irradiation and further incubation for 48 h. For viability assessment, Cells were stained with Calcein-AM (10 μg/mL) and PI (5 μg/mL), and then observed under CLSM. Moreover, Cell apoptosis was quantified by FCM after staining with Annexin V-FITC and 7-AAD.

CCK-8 assay kit was employed to assess dose-dependent cytotoxic effects. 22RV1 cells were incubated with the prepared NPs at varying concentrations, and then irradiation with NIR and incubation for 48 h. Cell viability was measured by microplate reader. Furthermore, cytotoxicity against HUVECs and RWPE-1 cells was evaluated at concentrations up to 160 μg/mL.

2.10.Antitumor mechanism of M/B@PDA-VHH NPs in vitro

Intracellular mitochondrial membrane potential and DNA damage were evaluated by JC-1 probes and comet assay. After the 22RV1 cells adhered, the initial culture medium was exchanged with fresh medium containing PBS, M/B@PDA, M@PDA-VHH, B@PDA-VHH and M/B@PDA-VHH for a further 6 h at 37 °C. After M/B@PDA-VHH+NIR treatment, Cell were incubated with JC-1 probe (5 μg/mL) and then imaged by CLSM.

To assess the DNA damage, M/B@PDA-VHH+NIR treated cells were mixed with low-melting-point agarose and loaded onto glass slides. After the agarose solidified, cells were lysed in pre-frozen alkaline buffer at 4 °C for 2 h. Under alkaline conditions (200 mM NaOH/1 mM EDTA, pH =13), electrophoresis was performed (at 25 V for 30 min), and stained with PI (2.5 μg/mL) and observed with CLSM.

The expression of key node proteins in the AKT/mTOR pathway was evaluated through Western Blot experiments. 22RV1 cells were treated with the previous NPs, and total protein within the 22RV1 cells were collected after the lysis process and quantified with a BCA protein assay kit. After electrophoresis, transfer and blocking , the membrane was incubated separately

with primary antibodies against AKT, p-AKT (Ser473), PRAS40, and p-PRAS40 (Thr246) at 4 °C overnight. After being washed with TBST, the membrane underwent incubation with the secondary antibody for 2 h at 25 °C. Immunoreactive bands were captured with a ChemiDoc imaging system (iBright CL750, USA).

2.11. In vivo target and tissue distribution of M/B@PDA-VHH NPs

The targeting effect of Cy5 labeled M/B@PDA-VHH NPs was in tumor-bearing mice, using M/B@PDA as controls. Animal experimental was approved by the Ethics Committee for Experimental Animals of the Affiliated Hospital of Guizhou Medical University. Briefly, Male BALB/c mice (5-week, 20 ± 2 g) were acclimatized for 1 week in specific pathogen-free facilities after procurement from Vital River Laboratories Co., Ltd. Tumor xenografts were established by subcutaneous injection of 100 μL serum-free suspension containing 1×10^6 22RV1 cells/mL. The mice were randomly allocated into three groups when the volumes reached about 100 mm^3. Then the mice received intravenous tail vein injections of Cy5-labeled M/B@PDA or M/B@PDA-VHH NPs. After 24h of NPs injection, tumors were irradiated with NIR and performed real-time thermal imaging. Mice from the M/B@PDA+NIR, M/B@PDA-VHH, and M/B@PDA-VHH+NIR groups were anesthetized and subjected to in vivo by a Xenogen IVIS spectrum imaging system (IVIS Lumina III, USA) at 2, 12 and 24 h. Following each imaging session, major organs (liver, spleen, heart, lungs, kidneys) and tumors were harvested and immediately imaged ex vivo as above. Following tissue harvest, samples were homogenized in ice-cold 0.5% Triton X-100 at 4 °C for a duration of 4 h. NPs content was quantified by measuring homogenate fluorescence intensity. The data were normalized to tissue weight and expressed as the percentage of injected dose per gram of tissue (%ID/g). To detect NO level, tumor-bearing mice received intratumoral injection of DAF-FM DA solution (20 μM) post-NIR irradiation. Tumors were harvested 1 h post-injection, and NO generation was analyzed in frozen sections using CLSM.

2.12. Antitumor efficacy and biosafety of M/B@PDA-VHH NPs in vivo

Therapeutic efficacy was assessed based on tumor growth inhibition and histopathological analysis. 22RV1 tumor-bearing mice were intravenously administered NPs suspensions and received local NIR irradiation (5 min) 24 h post-injection. Tumor volume and body weight were measured and recorded at two-day intervals until day 21. After treatment for 21 days, tumors and major organs were harvested, sectioned, and treated by hematoxylin and eosin (H&E) staining kit for pathological analysis. In addition, immunohistochemical (IHC) staining were performed in terms of AKT, p-AKT, PRAS40, p-PRAS40, Ki-67, and Cleaved Caspase-3, followed by observation under CLSM. Hematological and biochemical analyses were performed 24 h post-treatment to evaluate systemic safety. Complete blood counts, including white blood cells (WBC), red blood cells (RBC), hemoglobin (HGB), and platelets (PLT) were measured. Serum levels of alanine aminotransferase (ALT), aspartate aminotransferase (AST), blood urea nitrogen (BUN), and Creatinine (CREA) were analyzed to monitor cardiac, hepatic, and renal function. After the three-week treatment period, selected organs (liver, heart, spleen, kidney, and lung) were collected for histopathological.

2.13. Statistical analysis

All experiments data were showed as mean ± SD. All experiments data were showed as mean ± SD. Data analysis and comparison were calculated by one-way ANOVA and two-tailed Student's t-test. A p-value <0.05 was considered to be statistically.

3. Results and Discussion

3.1. Construction and Characterization of M/B@PDA-VHH NPs

Scheme 1a illustrates the fabrication process of M/B@PDA-VHH NPs. The PDA layer was assembled on PS core, and then the sacrificial PS layer was etched to obtain HPDA NPs. ML216

and BNN6 were then encapsulated with PCM and loaded into the HPDA cavity. Finally, VHH was grafted onto the surface to yield the M/B@PDA-VHH NPs. Fig. 1a displays TEM images of PS@PDA, HPDA-PS, HPDA, M/B@PDA, and M/B@PDA-VHH NPs after PDA coating for 12 h. The PDA was effectively deposition on PS core with shell thicknesses of~16 nm. The obtained PS@PDA NPs were then incubated in a 1% toluene/aqueous solution for 6 h. During this process, toluene absorption induced swelling of the PS core, generating internal pressure that ruptured the PDA shell upon exceeding a critical threshold. This controlled rupture created a single opening for polymer extrusion, forming HPDA NPs with a single pore (111 nm) [28]. Prolonging the PDA coating to 24 h yields a thicker shell (~30 nm) on the PS@PDA NPs compared to the 12 h treatment, while resulting in a relatively smaller single pore (~63 nm) in the final HPDA NPs (Fig. 1b). Previous reports showing that smaller pore could optimize the drug loading capacity and release kinetics of HPDA [15], thus the 24 h PDA coating was selected for subsequent study. After loading with ML216 and BNN6, M/B@PDA NPs exhibited a substantially enhanced internal contrast relative to the unloaded HPDA (Fig. 1b), confirming the successful co-loading of the PCM and the therapeutics.

Specifically, the PCM was formulated by blending lauric acid and stearic acid at a 4:1 weight ratio. The resulting composite exhibits a melting point at 39 °C, slightly above normal body temperature (37.8 °C), which facilitates thermally activated drug release [29]. The final step involved conjugating anti-PSMA nanobodies (VHH3) onto the M/B@PDA surface to produce actively targeted M/B@PDA-VHH NPs, showing no obvious morphology change after VHH3 grafting. However, the M/B@PDA NPs exhibited severe structural collapse and aggregation after drug loading, a trend that was further exacerbated following VHH modification (Fig. 1a). This progressive degradation strongly implied a failed encapsulation of PCM, which was critical for maintaining the mechanical strength of NPs [28]. SEM observation confirmed the presence of

significant internal voids and structural collapse in the NPs with 12 h coating (Fig. 1c). In contrast, M/B@PDA-VHH NPs presented intact spherical structures with clearly visible surface openings (Fig. 1d). These distinct morphological features collectively demonstrate the successful preparation of the M/B@PDA-VHH NPs. To assess the conjugation of VHH on M/B@PDA NPs, SDS-PAGE analysis was showed in Fig. 1e [30]. A characteristic 17 kDa band corresponding to VHH was observed in the M/B@PDA-VHH, confirming successful VHH immobilization [31]. The hydrodynamic sizes of PS@PDA, HPDA-PS, HPDA, M/B@PDA, and M/B@PDA-VHH NPs were around 231 ± 5 , 295 ± 3, 255 ± 3, 255 ± 5, and 396 ± 6 nm with size polydispersity indices of 0.337, 0.473, 0.074, 0.086, and 0.236, respectively. (Fig. 1f).

The zeta potentials of PS@PDA (-37.2 mV), HPDA-PS (-35.1 mV), and HPDA (-35.5 mV) remained relatively constant, and M/B@PDA NPs showed a slight increase to -25.7 mV. Notably, the conjugation with VHH significantly altered the surface charge, increased the zeta potential of M/B@PDA-VHH to -4.89 mV (Fig. 1g), which was ascribed to the neutralizing effect of VHH binding to the negatively charged PDA surface. The successful preparation of M/B@PDA was confirmed by XPS. The survey spectra of M/B@PDA NPs showed obvious signals for F, S element (Fig. 1h). As evidenced by the high-resolution spectra the characteristic peak at 687.8 eV was from F-C bond (Fig. S1a) [32], and the S2p peaks showed obvious peak at 164.7 eV correspond to a S – C bond (Fig. S1b) [33], The presence of the F and S elements is attributed directly to the F–C and S–C bonds derived from the ML216, thus confirming the successful loading of ML216. Further evidence was obtained from the high-resolution XPS spectrum of C1s (Fig. S1c), where the presence of the C–F bond (289.1 eV) and the C=O bond (286.8 eV) was also identified [34]. In addition, high-resolution XPS spectrum of C1s also presence of a C–N bond (285.9 eV), which coincided with that of the C–O bond. But the high-resolution XPS spectrum of N1s exhibited a distinct peak for the N=O bond between 402.3 eV [35], which

confirms the successful loading of BNN6 (Fig. S1d). The loading capacities of ML216 and BNN6 were 112 mg and 94 mg per gram of M/B@PDA-VHH NPs, respectively. And the size of M/B@PDA-VHH NPs demonstrated no evident alterations after incubation in PBS, culture medium, and serum for 7 days (Fig. 1i), confirming their stability for subsequent in vivo studies.

3.2. Photothermal and NO release properties of M/B@PDA-VHH NPs

Owing to its broadband absorption and non-radiative relaxation, PDA demonstrates exceptional NIR absorption capacity and photothermal conversion efficiency [36]. The concentration-dependent photothermal effect of HPDA NPs were presented in Fig. 2a. The temperature of HPDA NPs was positively correlated with their concentration from 0 to 300 μg/mL. Under 808 nm NIR irradiation, the solution temperature increased to 48.6 °C at 100 μg/mL, within the mild photothermal treatment range (Fig. 2b) which disrupts the dense tumor microstructure and maintain its superior safety [37]. Therefore, we further examined the power density of 808 nm NIR on the photothermal efficiency of 100 μg/mL HPDA NPs. The temperature of HPDA NPs exhibited a substantial increase with rising power density in the range of 0.5-2.5 W/cm² (Fig. 2c). Specifically, the temperature increased from 47.8 °C (1.5 W/cm^2) to 62.5 °C (2.5 W/cm^2), indicating the feasibility of achieving adjustable photothermal efficiency. Given that the phase transition temperature of the PCM is 39 °C, a condition that generates a temperature marginally above this melting point was considered optimal for efficient drug release. Consequently, a formulation of 100 μg/mL HPDA NPs irradiated under an 808 nm NIR with 1.5 W/cm² for 5 min was selected for subsequent experiments [16]. Given thermal stability and photothermal conversion efficiency constitute foundational metrics for PTT, directly governing its safety profile, treatment reliability treatment reliability, and procedural repeatability. we investigated the photothermal stability of M/B@PDA-VHH NPs (Fig. 2d). Over four on/off laser irradiation

cycles, the M/B@PDA-VHH NPs consistently reached about 47.3°C, indicating the PCM loading does not compromise the photothermal efficacy. Moreover, the photothermal performance of M/B@PDA-VHH NPs was systematically analyzed by monitoring their heating and cooling dynamics. The resultant data yielded a characteristic thermal time constant and a maximum equilibrium temperature, from which determined the photothermal conversion efficiency (η) to be 36% (Fig. 2e). These results suggest that M/B@PDA-VHH NPs as a promising candidate for PTT applications.

To characterize the NIR-triggered drug release profile, the cumulative release of ML216 from M/B@PDA-VHH NPs under NIR irradiation was monitored. As Fig. 2f illustrated, only minimal ML216 release (~5%) was detected without NIR exposure, owing to the solidified PCM matrix which effectively prevented premature drug leakage. Once the temperature reached exceeds the melting point of PCM, the system exhibited sustained ML216 release and over 37% cumulative release after incubation at 42 °C condition for 45 min. This demonstrates that drug release can be precisely governed by thermally controlling the PCM state [38]. The ML216 release kinetics demonstrated a strong dependence on the 808 nm NIR irradiation. A rapid release phase during each irradiation period was followed by a sustained slower release, culminating in a cumulative release of ~49 % over three cycles within 45 min. This might be attribute to the NPs rapidly convert the NIR light energy into heat energy, generating local high temperatures, and transformed the solid PCM into liquid. The residual heat in the system after the NIR was turned off promotes the continuous release of the drug [39]. The release of BNN6 is predicated on the cleavage of its intrinsic high-energy N-N bonds a process that can be initiated either by direct heating or through the absorption of photon energy [40]. We investigated the release of NO after NIR exposure (Fig. 2g). The results showed that NO can be continuously released under NIR exposure. The concentration of NO not only stabilized at a high level but also demonstrated a

gradual upward trend within 20 min. After three times intermittent NIR exposure, the cumulative release of NO increased to 64.4 μM within 45 min. Remarkably, the NO generation tracked the laser on/off cycling, demonstrating a controllable and stimuli-responsive release.

3.3. In Vitro Motion behavior and Penetration of M/B@PDA-VHH NPs

The gas-driven motion behaviors of M/B@PDA-VHH/NIR were examined by analyzing their motion trajectories, velocity, and MSD, using non-irradiated M/B@PDA-VHH NPs as controls. Motion trajectories were recorded in an engineered tumor extracellular matrix model by using a hyaluronan solution [41]. As a result of the absence of NO release, M/B@PDA-VHH NPs exhibited characteristic Brownian motion (Video S1), with random movement driven by thermal collisions of water molecules (Fig. 3a). However, M/B@PDA-VHH+NIR displayed nearly linear trajectories at the individual levels (Videos S2), whereas the motion directions diverged among NPs (Fig. 3a). This directional propulsion is attributed to the NO gas that is asymmetrically released from the Janus-structured NPs following photothermal activation. To quantitatively assess motion, the trajectories of 20 NPs were tracked to calculate the MSD [42]. As illustrated in Fig. 3b, the MSD of the NPs showed a linear dependence on time interval. Notably, the MSD values of M/B@PDA-VHH+NIR were substantially elevated compared to alone M/B@PDA-VHH NPs, confirming that NIR exposure effectively enhances diffusive motion. The mean velocity of M/B@PDA-VHH+NIR (7.09 μm/s) are approximately 4.5-fold higher than that of M/B@PDA-VHH NPs (1.57 μm/s) (Fig. 3c), attributing to the NO triggered self-propulsion after NIR irradiation [43].

Motivated by these discoveries, the penetration capabilities of the NPs were evaluated in 2D transvacular transwell and 3D 22RV1 tumor cells spheres. Specifically, The HUVEC was put at the upper layer and 22RV1 cells at the lower chamber, followed adding Rhodamine B labeled

M/B@PDA-VHH into upper chambers [44]. Fig. 3d presents CLSM images of the lower chamber 22RV1 cells with or without NIR irradiation. M/B@PDA-VHH treatment resulted in faint red fluorescence, indicating negligible penetration of the M/B@PDA-VHH NPs through the cellular barrier. In contrast, significantly enhanced red fluorescence was observed in the lower chamber after M/B@PDA-VHH+NIR treatment, demonstrating that NIR irradiation facilitated NPs across the HUVECs barrier towards the tumor cells. Furthermore, FCM revealed that NIR irradiation markedly increased nanoparticle internalization by 22RV1 cells in the lower chamber (26.5%) compared with the non-irradiated group (0.44%) (Fig. 3e). This improvement is attributed to NIR-triggered NO release, which propels the nanomotors and thereby facilitates trans-endothelial transport.

Fig. 3f showed the penetration depth of NPs across 3D 22RV1 tumor cells spheres with or without NIR treatment. Treatment with M/B@PDA-VHH alone resulted in limited penetration, reaching less than 40 μm into the spheroid. However, M/B@PDA-VHH/NIR showed significant penetration effect extends from the surface (0 μm) to the bottom (120 μm). The corresponding red fluorescence was nearly uniformly distributed across the largest cross-section, indicating homogeneous infiltration throughout the spheroid. The enhanced penetration results from NIR-triggered NO release to propels them deep into the tissue, highlighting the therapeutic potential of this nanoplatform against solid PCa.

3.4. In Vitro target and cellular uptake of M/B@PDA-VHH NPs

PSMA is a type II transmembrane glycoprotein with enzymatic activity. While minimally expressed in normal tissues, PSMA is significantly upregulated in malignant PCa, making it a promising molecular target for therapeutic intervention [45]. Anti-PSMA nanobodies (VHH) possess high binding affinity and rapid tissue penetration, rendering them ideal ligands for active tumor targeting. Using phage display technology, three anti-PSMA single-domain antibodies

(VHH2, VHH3, and VHH4) were screened by assessing the specific binding to 22RV1 cells (PSMA-positive), and PC3 cells (PSMA-negative) serving as a control. FCM analysis showed that VHH3 effectively binds to PSMA-positive 22RV1 cells with a positivity rate of 71.2% (Fig. 4a). In contrast, VHH2 and VHH4 showed minimal binding (2.84% and 5.11%, respectively), comparable to the negative control (1.92%). The limited efficacy of VHH2 and VHH4 may stem from lower molecular stability or poor recognition of natively folded PSMA [46]. In PSMA-negative PC3 cells, all nanobodies displayed negligible binding signals close to background levels. Collectively, these results confirm that VHH3 possesses strong and selective targeting capability toward PSMA-positive PCa cells.

The binding effect of VHH2, VHH3 and VHH4 grafted on M/B@PDA NPs were evaluated after incubation with Alexa Fluor 488-labeled PSMA protein. VHH3-functionalized NPs demonstrated significant retention of the fluorescent antigen than those of VHH2 and VHH4 modified NPs. (Fig. 4b), confirming that VHH3 maintains high PSMA affinity even after surface conjugation. Due to its superior performance, VHH3 grafted NPs were selected for all subsequent studies [47].

To investigate cellular internalization, 22RV1 cells were incubated with VHH3-grafted M/B@PDA-VHH NPs. As depicted in Fig. 4c, NPs internalization increased progressively over the first 12 h and plateaued thereafter, reaching a phagocytic efficiency of 40.1% after incubation for12 h. Fig. 4d summarizes CLSM images after dihydrochloride staining of 22RV1 cells. Treatment with M/B@PDA-VHH revealed a much brighter red fluorescence signal compared to the non-targeted M/B@PDA treatment, indicating high-affinity binding and precise recognition of tumor cells.

To verify that uptake is driven specifically by VHH-mediated targeting, competitive binding assays were performed. Pre-incubating M/B@PDA-VHH NPs with soluble PSMA antigen

blocked the VHH paratopes, allowing comparison with non-targeted M/B@PDA NPs [48]. CLSM analysis revealed strong red fluorescence in cells treated with M/B@PDA-VHH NPs (Fig. 4e), and weak fluorescence were observed after pre-blocked NPs with PSMA. This reduction indicates competitive inhibition of VHH-mediated internalization, as soluble PSMA occupies the binding sites and prevents interaction with membrane-bound PSMA on 22RV1 cells [19]. There no significant uptake difference in non-functionalized M/B@PDA NPs with or without PSMA pre-treatment. Quantitative fluorescence measurements revealed similar trends (Fig. 4f), highlighting the high target selectivity of M/B@PDA-VHH to PSMA positive 22RV1 cells.

3.5. In vitro safety evaluation

Biocompatibility is critical to advancing the biomedical application and clinical translation of M/B@PDA-VHH NPs. Quantitative CCK-8 assays demonstrated high cell viability (>90%) in both HUVEC and normal RWPE-1 after 24 h of exposure to M/B@PDA-VHH at concentrations up to 160 μg/mL, indicating negligible cytotoxicity toward normal cells (Fig. S2a). This was further corroborated by calcein-AM/PI live-dead staining, where both cell types exhibited exclusively green fluorescence, confirming preserved cellular viability and supporting the biocompatibility of the NPs (Fig. S2b). Hemocompatibility was evaluated through an in vitro hemolysis assay, a critical safety metric for intravenous administration [49]. The results showed minimal erythrocyte damage, with hemolysis rates below 5% at all tested concentrations (0–160 μg/mL) (Fig. S2c), confirming favorable blood compatibility and supporting further in vivo investigation.

3.6. In Vitro anti-PCa efficacy of M/B@PDA-VHH NPs

Exogenous NO and its derivatives mediate significant anti-tumor effects against PCa by directly inducing tumor cell apoptosis and cell cycle arrest, inhibiting proliferation and metastasis,

remodeling the immune microenvironment, and modulating the androgen receptor signaling pathway [50]. The NO generation in 22RV1 cells was assessed using DAF-FM DA. The red fluorescence in M/B@PDA-VHH+NIR was obvious stronger than those of other treatment (Fig. 5a), indicating effective NO generation. As quantified in Fig. 5b, there were undetectable fluorescence signals after PBS and M@PDA-VHH+NIR treatment, due to the absent of BNN6 loading. In contrast, the mean red fluorescence intensity of M/B@PDA-VHH+NIR was significantly higher than that of PBS treatment, indicating the NIR irradiation triggered NO release.

BLM, a member of the RecQ helicase family, plays key roles in DNA replication, repair, and telomere maintenance. Impairment of BLM activity is a known cause of genomic instability [13] , Small-molecule inhibitor ML216 promotes intracellular ROS accumulation by disrupting DNA repair and inducing genomic stress [51]. Intracellular ROS contents were determined with the green fluorescent probe DCFH-DA, oxidized into green-fluorescent DCF. As shown in Fig. 5c, relative to the weak signal in PBS-treated cells, treatment with M/B@PDA+NIR and M@PDA-VHH+NIR resulted in enhanced green fluorescence, with the M/B@PDA-VHH+NIR group showing the strongest intensity. Quantitative analysis showed no significant difference between the M/B@PDA-VHH (1.4 a.u.) and PBS (1.0 a.u.) groups (Fig. 5d), confirming minimal drug leakage without irradiation. Among NIR-exposed groups, M/B@PDA+NIR exhibited the lowest fluorescence (8.0 a.u.), attributable to limited cellular uptake without VHH targeting. The B@PDA-VHH+NIR group showed higher intensity (14.4 a.u.), likely due to NO-derived nitrosative stress [52]. Further increase in the M@PDA-VHH+NIR group (19 a.u.) may result from ML216-mediated impairment of DNA repair. The highest ROS level (28.2 a.u.) was achieved with M/B@PDA-VHH+NIR, reflecting the combined effect of concurrently released ML216 and NO.

The antitumor activity against 22RV1 cells was assessed by live/dead (calcein-AM/PI) staining following various treatments. As illustrated in Fig. 5e, while PBS treatment resulted in substantial live 22RV1 cells displaying green fluorescence, the M@PDA-VHH+NIR treatment induced a significantly enhanced red fluorescence in comparison to the other conditions. Apoptosis was further quantified by FCM (Fig. 5f). M/B@PDA-VHH 22RV1 treated cells exhibited a low apoptosis rate of 10.9%. Non-targeted PTT M/B@PDA+NIR induced 17.5% apoptosis. The incorporation of VHH targeting substantially improved efficacy, with apoptosis rates reaching 49.3% for M@PDA-VHH+NIR and 57.5% for B@PDA-VHH+NIR. The highest level of apoptosis (90.2%) was achieved with the combined M/B@PDA-VHH+NIR treatment, underscoring the synergistic effect of integrating PTT with NO and ML216.

Cytotoxicity was assessed via CCK-8 assay across a concentration range (0–160 μg/mL) (Fig. 5g). M/B@PDA-VHH NPs alone maintained >80% cell viability even at 160 μg/mL, confirming minimal toxicity without activation. Conversely, cell viability was notably reduced to 65.4% and 30.1% following treatment with M/B@PDA+NIR and M@PDA-VHH+NIR, respectively. Most notably, M/B@PDA-VHH+NIR treatment resulted in the lowest viability (7.2%), significantly lower than that of B@PDA-VHH+NIR (25.7%). This potent cytotoxicity is attributed to the NIR-triggered co-release of ML216 and NO. High concentrations of NO and its derivatives induce direct DNA damage and promote apoptosis [23]. Concurrently, ML216 inhibits BLM helicase, leading to replication fork arrest, double-strand break accumulation, impaired DNA repair, mitochondrial ROS burst, and amplification of NO-mediated damage, culminating in cell death [53].

3.7. Anti-PCa Mechanisms of M/B@PDA-VHH NPs

The potent cytotoxic effect of M/B@PDA-VHH NPs against 22RV1 cells prompted an

investigation into the underlying molecular mechanisms. Elevated intracellular levels of ROS and NO are known to disrupt mitochondrial integrity, leading to increased membrane permeability and loss of mitochondrial membrane potential [54]. JC-1 fluorescent probe was used to assess mitochondrial membrane potential. High potential promotes red J-aggregate formation, whereas diminished potential results in green monomer fluorescence. As shown in Fig. 6a, cells treated with M/B@PDA-VHH+NIR displayed markedly stronger green fluorescence compared to the PBS, M/B@PDA-VHH, M/B@PDA+NIR, M@PDA-VHH+NIR and B@PDA-VHH+NIR groups, indicating significant mitochondrial membrane potential depolarization and corroborating the pro-apoptotic effect. Quantitative analysis revealed that the red-to-green fluorescence intensity ratio in the M/B@PDA-VHH+NIR group was 21.2 times higher than that in the PBS control (Fig. 6b). Elevated ROS can directly induce oxidative damage on nuclear and mitochondrial DNA. The extent of DNA damage was subsequently evaluated via comet assay (Fig. 6c). M/B@PDA-VHH+NIR treatment showed obvious DNA comet tailing phenomenon, attributed to VHH-mediated phagocytosis and ROS-dependent DNA damage. Quantitative analysis revealed that PBS treatment showed 8.5% DNA migration (Fig. 6d). The most severe damage occurred in the M/B@PDA-VHH+NIR group with 57.7% tail DNA, significantly higher than those of M/B@PDA-VHH (9.9%), M/B@PDA+NIR (12.6%), M@PDA-VHH+NIR (37.1%) and B@PDA-VHH+NIR (46.6%) treatment. Collectively, these results demonstrate that the antitumor activity of M/B@PDA-VHH NPs under NIR irradiation primarily stems from the induction of severe mitochondrial dysfunction and DNA damage, driven by the intracellular accumulation of ROS and NO. Tumor cells can adapt to elevated ROS/NO stress by regulating survival gene expression, counteracting DNA damage, and evading apoptosis [55]. Our prior work demonstrated that BLM suppression modulates the AKT/mTOR pathway to mitigate oxidative damage [14]. We therefore examined whether the delivered BLM inhibitor ML216 regulates adaptive resistance by

suppressing the p-AKT and p-PRAS40.

Western Blot experiments analysis of 22RV1 cells showed that total AKT expression remained largely unchanged across all treatment groups (Fig. 6e). However, p-AKT was markedly affected, and M/B@PDA-VHH treatment resulted in p-AKT levels reduced to 80% compared to PBS treatment (Fig. 6f). NIR exposure significantly suppressed p-AKT to less than 60%, with M/B@PDA+NIR, M@PDA-VHH+NIR, and B@PDA-VHH+NIR reducing levels to 55.2%, 44.3%, and 10.0%, respectively. The most profound inhibition was observed with M/B@PDA-VHH+NIR, which decreased p-AKT to merely 0.6% of PBS treatment. These data indicate that the M/B@PDA-VHH/NIR potently suppresses AKT activation in PCa cells.

AKT activation phosphorylates PRAS40 at Thr246, leading to its dissociation from mTORC1 and subsequent activation of downstream pro-growth signaling [56]. Analysis of PRAS40 phosphorylation revealed that total PRAS40 levels were unaffected across all treatment groups (Fig. 6g). M@PDA-VHH+NIR and B@PDA-VHH+NIR reduced p-PRAS40 to 34.0% and 12.4% of PBS treatment, respectively (Fig. 6h). The most effective suppression was again achieved with M/B@PDA-VHH+NIR, which lowered p-PRAS40 expression to 3.3% of control. In summary, M/B@PDA-VHH+NIR treatment engages a dual mechanism against PCa. It significantly elevates intracellular ROS/NO, inducing mitochondrial depolarization and DNA damage. Concurrently, it potently suppresses the AKT/mTOR signaling axis, thereby disabling a key pathway that confers resistance to oxidative stress. This coordinated action results in potent therapeutic efficacy.

3.8. In vivo targeting and biodistribution of M/B@PDA-VHH NPs

Encouraged by its superior in vitro antitumor efficacy, we next evaluated the in vivo therapy potential of M/B@PDA-VHH+NIR. Photothermal images were captured after local NIR irradiation of tumors in differently treated mice (Fig. 7a). M/B@PDA-VHH+NIR treatment

induced a rapid temperature rise to 47.3 °C, attributable to efficient tumor accumulation and photothermal conversion. In the absence of NIR, M/B@PDA-VHH treatment showed no apparent temperature increase, remaining near body temperature (36.7 °C). M/B@PDA+NIR treatment exhibited lower tumor accumulation with the local temperature to 42.2 °C.

Real-time fluorescence imaging of live mice and ex vivo tissues were captured after intravenous injection of Cy5-labeled NPs, with or without NIR treatment (Fig. 7b). M/B@PDA+NIR treatment displayed weak fluorescence signals throughout the observation period, both M/B@PDA-VHH and M/B@PDA-VHH+NIR groups showed time-dependent fluorescence enhancement at the tumor site, indicating progressive accumulation of VHH-functionalized NPs. Ex vivo imaging confirmed predominant hepatic and renal uptake across all groups, yet M/B@PDA-VHH and M/B@PDA-VHH+NIR treatments exhibited clear tumor-selective aggregation, demonstrating VHH mediated tumor targeting. Fig. 7c summarized quantitative fluorescence intensity at tumor tissue. M/B@PDA-VHH+NIR showed 3.1 times higher significant fluorescence signal than that of M/B@PDA-VHH treatment, indicating NIR-triggered self-propelled motion contributed significantly to the enhanced tumor accumulation. In addition, M/B@PDA-VHH+NIR showed 8.0 times higher fluorescence intensity than that of passive accumulation (M/B@PDA-VHH). A significant enhancement in tumor accumulation of the NPs was verified, mediated by VHH targeting. Ex vivo tissue quantification corroborated these results, showing that VHH-functionalized NPs achieved 4.0-fold higher tumor fluorescence than passive carriers (Fig. 7d), which was further elevated to 6.9-fold under NIR irradiation.

Fig. 7e shows the biodistribution of NPs 2 h post-injection. NPs showed a broad distribution across major organs. Uptake was predominantly higher in the liver and kidneys, attributable to the reticuloendothelial system.The slightly negative surface charge contributed to prolonged blood circulation and fostered greater tissue accumulation of the NPs.

In addition, tumor irradiation (NIR, 5 min) was performed at 2 h post-injection. The 24h biodistribution data across treatment groups are summarized in Fig. 7f, revealing a significant decrease in NP levels within most tissues relative to the 2h, indicative of time-dependent systemic clearance. In contrast, tumor accumulation increased. This enhancement is attributed to the NO-induced vasodilation coupled with elevated blood flow from mild PTT, which improve NPs penetration and retention. As shown in Fig. 7f, Compared with M/B@PDA-V+HH alone, the combination of VHH targeting, photothermal-propelled motion, and NO release in the M/B@PDA-VHH+NIR group increased tumor NPs levels by approximately 1.2-fold. Moreover, the lack of active targeting in the M/B@PDA+NIR group resulted in about 1.3-fold higher accumulation relative to non-targeted M/B@PDA-VHH. These results verify that tumor accumulation is substantially enhanced by the synergistic actions of VHH-mediated targeting, persistent self-propulsion, and NO release.

Intratumoral NO generation was assessed by CLSM following local injection of the NO-sensitive probe DAF-FM DA. As shown in Fig. 7g, M/B@PDA-VHH+NIR treatment showed strong green fluorescence, indicating substantial NO production upon NIR illumination. Fig.7h presents the fluorescence intensities of stained sections from ImageJ analysis. The faint signals were observed after M/B@PDA+NIR (5.0 a.u.) and M/B@PDA-VHH (9.3 a.u.) treatment, reflecting limited NO release. In contrast, the M/B@PDA-VHH+NIR group (31.8 a.u.) exhibited intense and homogeneous green fluorescence across tumor sections, confirming robust and widespread NO generation. These results indicate that M/B@PDA-VHH NPs retain their payload stably during tumor penetration prior to irradiation. Subsequent NIR exposure triggers the concurrent release of BNN6 and ML216, leading to localized NO production and enabling potent synergistic therapy against PCa.

673 *3.9. In vivo antitumor efficacy of M/B@PDA-VHH NPs*

674 The antitumor efficacy of M/B@PDA-VHH+NIR (group #6) was evaluated by monitoring body
675 weight, tumor volume, tumor weight, and histopathological and IHC staining, with PBS (group
676 #1), M/B@PDA-VHH (group #2), M/B@PDA+NIR (group #3), M@PDA-VHH+NIR (group #4),
677 and B@PDA-VHH+NIR (group #5) as controls. As illustrated in Fig. 8a, the body weight
678 maintained a steady upward trajectory across all groups. The greatest weight increase was
679 observed in the M/B@PDA-VHH+NIR group, indicating that the combined treatment did not
680 induce overt systemic toxicity. Fig. 8b summarized tumor growth after various treatments.
681 Tumors in PBS-treated mice grew rapidly from 100 to approximately 1165 mm^3 over 21 days,
682 while M@PDA-VHH treatment showed no inhibitory effect. The combination of PTT and
683 M216/NO mediated M/B@PDA+NIR through passive EPR accumulation, reducing the final
684 tumor volume to approximately 639 mm^3 [57]. M@PDA-VHH+NIR apparently inhibited tumor
685 expansion to about 419 mm^3, ascribed from PTT/ML216 synergetic effect. NO/PTT therapy after
686 B@PDA-VHH+NIR traetment exhibited remarkable tumor inhibition, maintaining a volume of
687 approximately 100 mm^3 throughout the 21-day study period [58]. Tumor growth was completely
688 suppressed by M/B@PDA-VHH+NIR, and the tumor volume even decreased throughout the
689 experimental period. Following the experiment, mice were euthanized for subsequent tumor
690 resection and gravimetric analysis. As showed in Fig. 8c, M/B@PDA-VHH+NIR treatment
691 reduced tumor weight to 0.056 g, which was significantly lower than that of M/B@PDA-VHH
692 (0.877 g), M/B@PDA+NIR (0.645 g), M@PDA-VHH+NIR (0.449 g), B@PDA-VHH+NIR
693 (0.123 g), and PBS (1.514 g) groups. Representative ex vivo tumor images are displayed in Fig.
694 8d, visually confirming the potent growth inhibition achieved by M/B@PDA-VHH+NIR.

695 To evaluate treatment outcomes, histopathological analysis via H&E staining was performed
696 on tumor tissues harvested on day 21. Compared to all other treatments, M/B@PDA-VHH+NIR

induced the most severe tumor destruction, characterized by enlarged necrotic regions, cellular disintegration, cytoplasmic degradation, extensive coagulative necrosis, and complete loss of tissue architecture (Fig. 8e). Apoptosis and proliferation of the tumor tissue were evaluated by IHC detection of caspase-3(Fig. 8f) and Ki67 expression (Fig. 8g). PBS treated tumors displayed high Ki67 positivity and minimal caspase-3 expression, indicating active proliferation. In contrast, M/B@PDA-VHH+NIR treatment resulted in the highest level of apoptosis and the lowest proliferative activity, demonstrating that the combination of PTT with NO and ML216 delivery produces superior antitumor efficacy in PCa.

The in vivo expression levels of the pivotal AKT/mTOR node proteins AKT, p-AKT, PRAS40 and p-PRAS40 were subsequently examined after various treatment. Immunofluorescence staining of tumor sections revealed the distribution and intensity of AKT (Fig. 8h) and p-AKT (Fig. 8i). Total AKT levels showed no appreciable change across groups (Fig. S3a). Strong p-AKT immunoreactivity (red) was observed in PBS-treated tissues, with similar signals in the M/B@PDA-VHH and M/B@PDA+NIR groups, indicating no significant reduction in p-AKT expression (Fig. S3b). A stepwise decrease in red fluorescence was seen in the M@PDA-VHH+NIR and B@PDA-VHH+NIR treatment, and the signal was nearly abolished in the M/B@PDA-VHH+NIR treatment. These results demonstrate that while total AKT expression remained unaltered, p-AKT was significantly inhibited by the M/B@PDA-VHH+NIR treatment. This selective suppression is functionally relevant because p-AKT represents the active phosphorylated form that drives downstream signaling to regulate cell survival, proliferation, metabolism, and migration [59].

PRAS40 is a key regulatory node within the AKT/mTOR signaling cascade. Its activity is modulated by site-specific phosphorylation, primarily catalyzed by activated p-AKT. In its unphosphorylated state, PRAS40 binds competitively to RAPTOR, inhibiting mTORC1 activity

and suppressing oncogenic proliferation. p-AKT converts PRAS40 to p-PRAS40, triggering its dissociation from mTORC1 and thereby reactivating the pathway to promote tumor progression [60]. Immunofluorescence staining of tumor sections was performed to evaluate PRAS40 (Fig. 8j) and p-PRAS40 (Fig. 8k) expression following in vivo treatments. Total PRAS40 levels showed no significant difference across groups (Fig. S3c). Similarly, p-PRAS40 signal remained unchanged after M/B@PDA-VHH treatment compared to the PBS control. M/B@PDA-VHH +NIR showed significant diminished red fluorescence to 3.9 %, lower than that of B@PDA-VHH+NIR (31.2%), M@PDA-VHH+NIR (44.4%), M/B@PDA+NIR (64.6%), M/B@PDA-VHH (98.9%), and PBS (100%) treatment (Fig. S3d). These in vivo results confirm the potent antitumor activity of M/B@PDA-VHH under NIR irradiation. The NIR-triggered co-release of NO and ML216 selectively inhibits the phosphorylation and activation of p-AKT and p-PRAS40, key effectors in the DNA damage-responsive AKT/mTOR pathway. This dual blockade overcomes therapeutic resistance, sustains DNA damage, and ultimately enhances treatment outcomes in PCa.

3.10. Treatment safety of M/B@PDA-VHH NPs

To evaluate the in vivo biosafety of M/B@PDA-VHH+NIR, hematological, biochemical, and histopathological analyses were performed after 14 days of treatment. Comprehensive blood testing showed that WBC (1.2×10^9/L),RBC (7.6×10^{12}/L), HGB (124 g/L), and PLT (7.8×10^{11} /L) remained within the physiological ranges even at a dose of 30 mg/kg, indicating no adverse systemic effects (Fig. S4a). Serum biochemical markers, including ALT (29.2 U/L), aspartate AST (127.4 U/L), BUN (23.5 mg/dL), and CREA (32.5 μmol/L), also fell within normal limits, confirming an absence of hepatorenal toxicity (Fig. S4b). Furthermore, H&E staining of major organs revealed almost no structural damage, necrosis, or inflammatory infiltration in any treatment group compared to PBS-treated controls (Fig. S5). Together, these results demonstrate

that M/B@PDA-VHH+NIR treatment induces no significant toxicity in normal tissues, supporting its favorable biosafety profile.

4. Conclusion

This study developed a NIR-propelled, PSMA-targeting nanomotor platform for enhanced deep tumor penetration and synergistic PCa therapy. The system co-encapsulated the BLM helicase inhibitor ML216 and a NO donor within a temperature-responsive PCM, loaded into single-pore hollow PDA NPs. Under NIR irradiation, efficient photothermal conversion triggered the controlled release of both NO and ML216. The released NO served a dual function as a cytotoxic agent and a gas propellant, significantly enhancing NPs motion and penetration across endothelial barriers, 3D tumor spheroids, and in vivo tissues. Concurrently, the synergistic action of PTT and NO induced DNA damage and promoted apoptosis in cancer cells. The co-released ML216 inhibited BLM helicase activity, leading to replication fork arrest, accumulation of double-strand breaks, and suppression of the AKT/mTOR survival pathway via dephosphorylation of p-AKT and p-PRAS40. This dual mechanism disrupted DNA repair networks, amplified oxidative damage, and restored therapeutic sensitivity. Both in vitro and in vivo studies confirmed potent tumor suppression with negligible systemic toxicity. This study exhibits a gas-propelled nanomotor strategy that synergistically combines deep tumor penetration with DNA damage repair interference, offering a promising approach to overcome stromal barriers and therapy resistance in solid tumors.

Acknowledgements

This work was co-supported by the National Natural Science Foundation of China [grant numbers 82360558, 82560969]; the Science and Technology Foundation of Guizhou Province [grant number MS [2025] 489]; the Guizhou Province Youth Science and Technology Talents

Growth Project [grant number Foundation-[2024] Youth 296]; the Foundation of Health Commission of Guizhou Province [grant number-gzwkj2021-534]; Youth Fund of Guizhou Provincial People's Hospital [grant number-GZSYQN[2022]13].

Data availability

All data included in this study are available upon request by contact with the corresponding author.

Declaration of Competing Interests

The authors declare that they have no known competing financial interests or personal relationships that could have appeared to influence the work reported in this paper.

References

[1] T. B. Kratzer, N. Mazzitelli, J. Star, W. L. Dahut, A. Jemal, R. L. Siegel, Prostate cancer statistics 2025, CA Cancer J Clin., 75 (2025) 485-497.

[2] Pinsky, Paul F., H. Parnes., Screening for prostate cancer, N. Engl. J. Med., 388 (2023) 1405-1414.

[3] D. Chakrabarti, P. Albertsen, A. Adkins, A. Kishan, V. Murthy, C. Parker, A. Pathmanathan, A. Reid, O. Sartor, N. Van As, J. Walz, A. Tree, The contemporary management of prostate cancer, CA Cancer J Clin., 75 (2025) 552-586.

[4] A. Barve, W. Jin, K. Cheng, Prostate cancer relevant antigens and enzymes for targeted drug delivery, J. Controlled Release, 187 (2014) 118-132.

[5]]B. Ghaemi, A. Rosu, S. Kuddannaya, G. Laurent, R. Bazzi, S. Roux, A. Shakeri-Zadeh, J. W. M. Bulte, MPI-guided photothermal therapy of prostate cancer using stem cell delivery of magnetotheranostic nanoflowers, Adv. Funct. Mater., 35 (2026) e21864

[6] X. Yu, Y. He, J. Zhong, Y. Li, Y. Zhu, Y. Chen, J. Yin, Z. Yuan, P. Yin, Immediate tumor killing and long-term anti-tumor immunoreaction induced by Bufalin-loaded phototherapeutic Janus membrane in CRC postoperative therapy, Mater. Today Bio., 37 (2026) 102824.

[7] W. Jiang, Z. Guo, Q. Wang, Z. Chen, W. Dong, Q. Liang, Y. Hao, H. Pan, C. Zeng, H. Liu, Y. Wang, Enhanced nanoparticle delivery across vascular basement membranes of tumours using nitric oxide, Nat. Biomed. Eng., 9 (2025) 1486-1501.

[8] H. Lu, B. Liang, A. Hu, H. Zhou, C. Jia, A. Aji, Q. Chen, Y. Ma, W. Cui, L. Jiang, J. Dong, Engineered biomimetic cancer cell membrane nanosystems trigger GAS-immunometabolic therapy for spinal-metastasized tumors, Adv. Mater., 37 (2025) 2412655.

[9] S. Liang, Y. Liu, H. Zhu, G. Liao, W. Zhu, L. Zhang, Emerging nitric oxide gas-assisted cancer photothermal treatment, Exploration, 4 (2024) 20230163.

[10] Q. Guo, J. Wang, J. Guo, Q. Wu, S. Li, H. Wang, Y. Sun, H. Liu, Biomedical micro/nanomotors: Driven mechanism, preparation and physiological barriers breakthrough, Coord. Chem. Rev., 530 (2025) 216441.

[11] Z. Ma, L. Chen, Y. Xi, K. Zhang, Y. Liu, W. Zhong, Y. Liu, C. Zheng, Y. Zhao, NO-driven self-propelled nanomotors augment chemo-immunotherapy and transcatheter arterial embolization, ACS Nano, 19 (2025) 28784-28880.

[12] C. Macedo-Silva, V. Miranda-Gonçalves, N. T. Tavares, D. Barros-Silva, J. Lencart, J. Lobo, Â. Oliveira, M. P. Correia, L. Altucci, C. J. S. t. Jerónimo, Epigenetic regulation of TP53 is involved in prostate cancer radioresistance and DNA damage response signaling, Signal Transduction Targeted Ther., 8 (2023) 395.

[13] E. Ledet, E. S. Antonarakis, C. Pritchard, W. B. Isaacs, A. O. Sartor, Germline heterozygous BLM mutations and prostate cancer risk, J. Clin. Oncol., 37 (2019) 321.

[14] K. Chen, H. Xu, J. Zhao, Bloom syndrome protein activates AKT and PRAS40 in prostate cancer cells, Med. Cell. Longevity, 2019 (2019) 3685817.

[15] J. Qiu, J. Xu, Y. Xia, Nanobottles for controlled release and drug delivery, Adv. Healthcare Mater., 10 (2021) 2000587.

[16] J. Qiu, D. Huo, J. Xue, G. Zhu, H. Liu, Y. Xia, Encapsulation of a phase-change material in nanocapsules with a well-defined hole in the wall for the controlled release of drugs, Angew. Chem. Int. Ed., 58 (2019) 10606-1061.

[17] L. T. Nordquist, E. Lengyelova, A. Iagaru, B. R. Mancini, H. Song, M. Osman, D. Josephson, F. Almaguel, D. Saltzstein, M. Parker, R. M. Miller, N. D. Shore, Sabre: Assessment of safety and efficacy of 64Cu-SAR-BBN in patients with PSMA-negative biochemical recurrent prostate cancer, J. Clin. Oncol., 42 (2024) TPS346.

[18] L. Maksymova, Y. A. Pilger, L. Nuhn, J. A. J. M. C. Van Ginderachter, Nanobodies targeting the tumor microenvironment and their formulation as nanomedicines, Mol. Cancer, 24 (2025) 65.

[19] L. Liu, B. Tu, Y. Sun, L. Liao, X. Lu, E. Liu, Y. Huang, Nanobody-based drug delivery systems for cancer therapy, J. Controlled Release, 381 (2025) 113562.

[20] R. H. Kang, M. Rasoulianboroujeni, M. Kianpour, L. Repp, S. M. Ponik, G. S. Kwon, Precise ratiometric drug delivery for the treatment of triple-negative breast cancer, ACS Nano, 19 (2025) 40456-40472.

[21] Z. Li, T. Li, S. Chen, J. Zhu, Friends fight the foes: Synergistic low-temperature photothermal/chemo/gas therapy for conquering cancer cells, Adv. Funct. Mater., 36 (2026) e14605.

[22] F. Li, K. Huang, H. Chang, Y. Liang, J. Zhao, S. Yang, F. Liu, A polydopamine coated nanoscale FES theranostic platform for the elimination of drug-resistant bacteria via

photothermal-enhanced fenton reaction, Acta Biomaterialia, 150 (2022) 380-390.

[23] Z. Shen, W. Jiang, S. Zheng, S. Luo, Z. Guo, Q. Wang, Y. Wang, J. Hu, Intracellular co-delivery of carbon monoxide and nitric oxide induces mitochondrial apoptosis for cancer therapy, Angewandte Chemie International Edition, 64 (2025) e202419939.

[24] S. Dutta, S. Sen, in Springer, Preparation and characterization of collagen-hyaluronic acid (Col-HA) matrices: in vitro mimics of the tumor microenvironment, Methods Mol. Biol. 2747 (2024) 131-139.

[25] S. Chen, D. E. Fan, P. Fischer, A. Ghosh, K. Göpfrich, R. Golestanian, H. Hess, X. Ma, B. J. Nelson, T. Patiño Padial, J. Tang, K. Villa, W. Wang, L. Zhang, A. Sen, S. Sánchez, A roadmap for next-generation nanomotors, Nature Nanotechnology, 20 (2025) 990-1000.

[26] D. Taylor, V. Forsyth, C. Riddering, A. R. Ariosa, Lipid nanoparticle screening in 2D vs 3D cultures: Ovarian cancer cell lines exhibit different preference for optimal lipid formulation in monolayers vs spheroids, Cancer Research, 85 (2025) LB185.

[27] D. Iyer, A. Bonteanu, J. Z. Zhu, P. Shepherd, R. Kittles, N. M. Navone, D. A. Harrington, D. Dexter, K. M. Bircsak, Development of a 3D in vitro model of the prostate tumor microenvironment, Cancer Research, 81 (2021) 2641.

[28] J. Qiu, Y. Shi, Y. Xia, Polydopamine nanobottles with photothermal capability for controlled release and related applications,Adv. Mater., 33 (2021) 2104729.

[29] C. Zhu, D. Huo, Q. Chen, J. Xue, S. Shen, Y. Xia, A eutectic mixture of natural fatty acids can serve as the gating material for near-infrared-triggered drug release, Advanced Materials, 29 (2017) 1703702.

[30] S. Yi, K. Noh, H. Kim, E. Jung, S. Kim, J. Lee, K. Guk, J. Choi, E.-K. Lim, S. J. M. C. Kim, Advancing pancreatic cancer therapy by mesothelin-specific nanobody conjugation, Mol. Cancer, 24 (2025) 124.

[31] Y. Dai, Z. Guo, D. Leng, G. Jiao, K. Chen, M. Fu, Y. Liu, Q. Shen, Q. Wang, L. Zhu, Q. Zhao, Metal-coordinated NIR-II nanoadjuvants with nanobody conjugation for potentiating immunotherapy by tumor metabolism reprogramming, Adv. Sci., 11 (2024) 2404886.

[32] F. Capone, J. Sottmann, V. Meunier, L. P. Ramírez, A. Grimaud, A. Iadecola, M. Scardamaglia, J.-P. Rueff, R. J. E. Dedryvère, E. Science, Operando observation of the dynamic SEI formation on a carbonaceous electrode by near-ambient pressure XPS, Energy Environ. Sci., 17 (2024) 1509-1519.

[33] Z. Liu, Y. Zhang, Y. Wu, B. Yang, Z. Zhou, Z. Jin, In situ XPS evidence of fully conjugated COF and C3N4 construct s-scheme heterojunction boosting photogenerated carriers transfer and separate for efficiently photocatalytic hydrogen evolution, Chin. J. Met. Sci. Technol., 233 (2025) 48-57.

[34] Y. Ku, G. Kim, M. Kim, H. Ahn, J.-K. Lee, J. Kim, B.-G. Park, D. Moon, S. Lee, S. Lee, Y. H. Jang, B. J. Jung, H. Kim, C. Lee, S.-M. Hur, J. Y. Park, C. Koh, T. Nishi, H.-W. Kim, Tin-oxo nanocluster extreme uv photoresists equipped with chemical features for atmospheric stability and high euv sensitivity, Adv. Funct. Mater., (2025) e25300.

[35] H. Zhuo, X. Liu, C. Sun, Y. Liu, J. Deng, X. He, P. Chen, Z. Li, J. Liang, Q. J. M. H. Xiong, An amino-functionalized lanthanide-organic framework for ratiometric detection of ONOO−, Mater. Horiz., 12 (2025) 7402-7408.

[36] C.-Y. Shi, S.-S. Yan, Y. Zhang, S.-H. Qiu, Q. Zhang, D.-H. Qu, Thioctic acid-grafted polydopamine nano-crosslinker with enhanced photothermal efficiency, Adv. Funct. Mater., (2025) e23360.

[37] M.-H. Qi, D.-D. Wang, W. Qian, Z.-L. Zhang, Y.-W. Ao, J.-M. Li, S.-W. Huang, High-efficiency gold nanoaggregates for NIR led-driven sustained mild photothermal therapy achieving complete tumor eradication and immune enhancement, Adv. Mater., 37 (2025)

2412191.

[38] B. Shi, N. Ren, L. Gu, G. Xu, R. Wang, T. Zhu, Y. Zhu, C. Fan, C. Zhao, H. Tian, Theranostic nanoplatform with hydrogen sulfide activatable nir responsiveness for imaging-guided on-demand drug release, Angew. Chem. Int. Ed., 58 (2019) 16826-16830.

[39] Y. Xie, Z. Yang, H. Shen, J. Chen, D. A. Weitz, D. Chen, J. Sheng, T. Liang, Interfacial engineering of biocompatible nanocapsules for near-infrared-triggered drug release and photothermal therapy, Adv. Sci., 12 (2025) 2410844.

[40] W. Bao, J. Meng, T. Li, Q. Li, H. Liu, Z. Tian, MOFs-based nanoinducer enables excessive autophagy for synergistic photoimmunotherapy, Small, 21 (2025) 2503848.

[41] J. Ou, K. Liu, J. Jiang, D. A. Wilson, L. Liu, F. Wang, S. Wang, Y. Tu, F. Peng, Micro-/nanomotors toward biomedical applications: the recent progress in biocompatibility, Small, 16 (2020) 1906184.

[42] T. Patiño Padial, S. Chen, A. C. Hortelão, A. Sen, S. Sánchez, Swarming intelligence in self-propelled micromotors and nanomotors, Nat. Rev. Mater., 10 (2025) 947-963.

[43] H. Zhang, K. Cao, C. Wang, Y. Tian, L. Hou, Thrombin and NIR dual-responsive system driven by heat-gas for thrombus targeted therapy, Chem. Eng. J., 498 (2024) 155054.

[44] M. Wan, Q. Wang, X. Li, B. Xu, D. Fang, T. Li, Y. Yu, L. Fang, Y. Wang, M. Wang, F. Wang, C. Mao, J. Shen, J. Wei, Systematic research and evaluation models of nanomotors for cancer combined therapy, Angew. Chem. Int. Ed., 59 (2020) 14458-14465.

[45] M. Fahrner, C. Zamboglou, S. K. B. Spohn, B. Oerther, T. Fechter, M. T. Freitag, C. Gratzke, P. Bronsert, O. Schilling, A.-L. Grosu, Advancing radioproteomics: Integration of prostate-specific membrane antigen positron emission tomography/computed tomography and multiparametric magnetic resonance imaging with localized proteomic profiling in prostate cancer, Eur. Urol., 88 (2025) 525-527.

[46] Z. Liu, J. Zhou, J. Liu, C. Zhao, Z. Cui, Q. Wang, W. Ma, X. Ma, F. Tang, X. Wang, Y. Li, D. Zhi, D. Wang, Anti-SV2C single domain nanobodies for molecular imaging in androgen receptor positive prostate cancer, Nano Today, 65 (2025) 102846.

[47] B. Van de Broek, N. Devoogdt, A. D'Hollander, H.-L. Gijs, K. Jans, L. Lagae, S. Muyldermans, G. Maes, G. Borghs, Specific cell targeting with nanobody conjugated branched gold nanoparticles for photothermal therapy, ACS Nano, 5 (2011) 4319-4328.

[48] J. Wu, H. Lu, X. Xu, L. Rao, Y. Ge, Engineered cellular vesicles displaying glycosylated nanobodies for cancer immunotherapy, Angew. Chem. Int. Ed., 63 (2024) e202404889.

[49] Q. Zheng, Y. Wang, D. E. Scott, Evaluation of hemolytic complications of intravenous immunoglobulin products using both intravascular and extravascular hemolysis assays, Blood, 144 (2024) 5594.

[50] A. Dey, J. Lee, M. Park, F. Ghahari, T. Ghosh, V. H. Duong, J. H. Park, ROS-responsive self-immolative polymeric prodrug for nitrosative stress-mediated cancer therapy, J. Controlled Release, 391 (2026) 114642.

[51] E. Viziteu, Y. L. Lin, L. Vincent, A. Seckinger, D. Hose, A. Constantinou, B. Klein, P. Pasero, J. Moreaux, A small molecule that selectively targets BLM helicase has a therapeutic interest in multiple myeloma, Blood, 128 (2016) 4433.

[52] Y. Li, T. Gong, H. Gao, Y. Chen, H. Li, P. Zhao, Y. Jiang, K. Wang, Y. Wu, X. Zheng, W. Bu, ZIF-based nanoparticles combine X-ray-induced nitrosative stress with autophagy management for hypoxic prostate cancer therapy, Angew. Chem. Int. Ed., 60 (2021) 15472-15481.

[53] X.-Y. Ma, J.-F. Zhao, Y. Ruan, W.-M. Zhang, L.-Q. Zhang, Z.-D. Cai, H.-Q. Xu, ML216-induced BLM helicase inhibition sensitizes PCa cells to the DNA-crosslinking agent cisplatin. Molecules, 27 (2022) 8790.

[54] T. Busenbender, S. Dyshlovoy, M. Kaune, L. Boeckelmann, T. Lange, U. Schumacher, D. N. Pelageev, Y. E. Sabutskii, K. Borisova, V. P. Anufriev, M. Graefen, C. Bokemeyer, G. Von Amsberg, In vitro and in vivo investigations of novel 1,4-napthoquinone sulphomethylene carbohydrate conjugates in prostate cancer, J. Clin. Oncol., 39 (2021) 104.

[55] A. K. Augspach, M. Rubin, P. Francica, S. Rottenberg, R. Kanadia,Targeting minor splicing disrupts DNA repair and overcomes therapy resistance in prostate and breast cancer, Cancer Res., 86 (2026) B003.

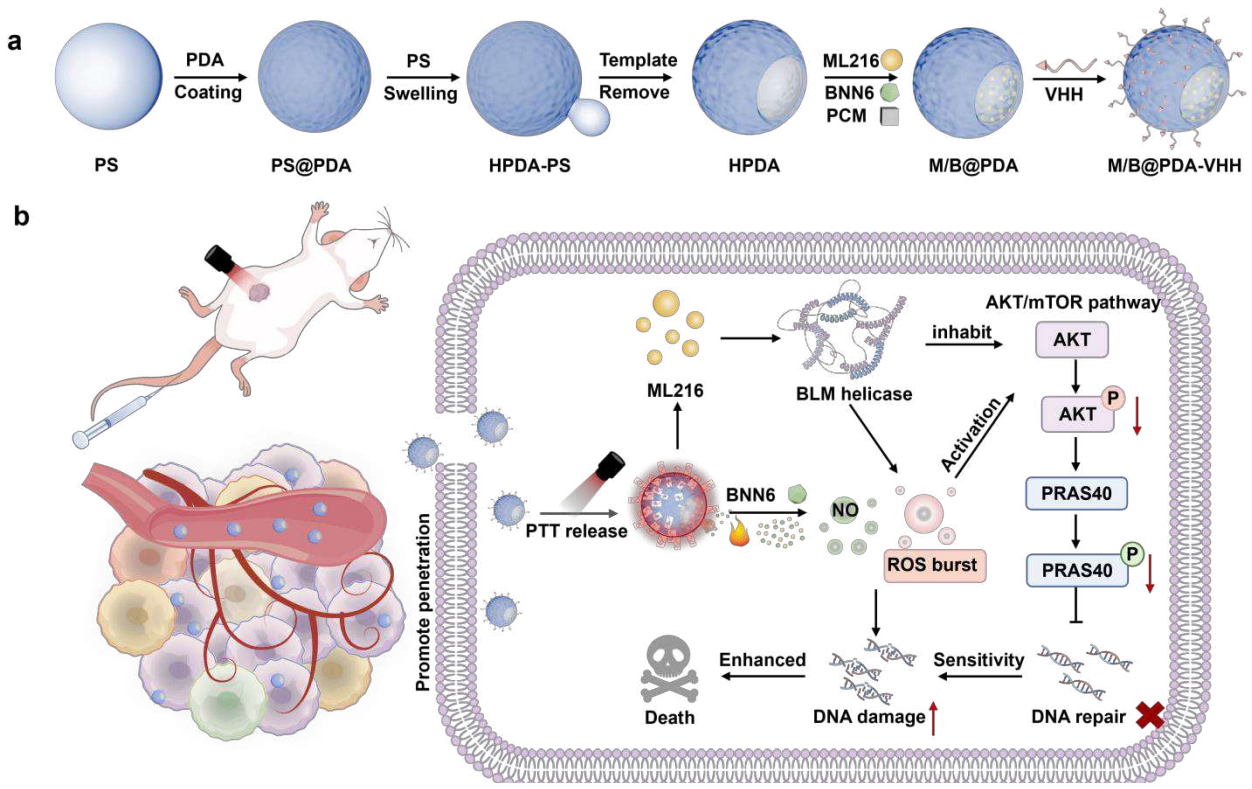
[56] M. A. De Velasco, Y. Kura, K. Sakai, S. T. Barry, C. Eberlein, C. Rooney, K. Nishio, K. Fujita, H. Uemura, Enhancing chemotherapy efficacy in PTEN-deficient prostate tumors with targeted AKT inhibition, Cancer Res., 85 (2025) 1686.

[57] Q. Dai, Z. Zhang, Z. Ben, X. Sun, Y. Yang, Y. Qin, Q. Yang, X. Bao, L. Wu, R. Jiang, X. Tan, X. Ying, S. Wang, Z. Li, Z. Yang, M. Han, Q. Wei, A regulatory biomimetic nanoparticle targeting senescent glioma cells for BNCT treatment, Chem. Eng. J., 532 (2026) 174453.

[58]]A. Mohanty, A. Mohapatra, A. Sundaram, P. Sathiyamoorthy, W. Park, S. K. Rajendrakumar, I.-K. Park, Triple-action cancer therapy using laser-activated no-releasing metallomicellar nanophotosensitizer for pyroptosis-driven immune reprogramming, J. Controlled Release, 379 (2025) 147-163.

[59] F. Song, C.-G. Wang, T.-L. Wang, Y.-C. Tao, J.-Z. Mao, C.-W. Hu, Y. Zhang, P.-J. Tang, C.-L. Lu, H.-L. Qing, L. Han, Z. Chen, Enhancement of gemcitabine sensitivity in intrahepatic cholangiocarcinoma through saikosaponin-a mediated modulation of the p-AKT/BCL-6/ABCA1 axis, Phytomedicine, 133 (2024) 155944.

[60] L. Yu, J. Wei, P. Liu, Attacking the PI3K/AKT/mTOR signaling pathway for targeted therapeutic treatment in human cancer, Cancer Biol., 85 (2022) 69-94.



Scheme 1. Preparation and Therapeutic Mechanism of the M/B@PDA-VHH NPs. (a) The PS core was coated with a PDA layer, and then the sacrificial PS layer was etched to obtain HPDA NPs. NO donor BNN6 and BLM helicase inhibitor ML216 were co-encapsulated with a PCM into the HPDA cavity, and then grafting with VHH3 to yield the M/B@PDA-VHH NPs. (b) Systemic administration of M/B@PDA-VHH NPs enhanced tumor accumulation via VHH targeting. Under NIR irradiation, the photothermal effect melts the PCM, triggering NO release, promoting deep tumor penetration of the NPs. The combined photothermal/NO therapy induces DNA damage, while ML216 inhibits the AKT pathway to suppress DNA repair, thereby synergistically enhancing tumor eradication.

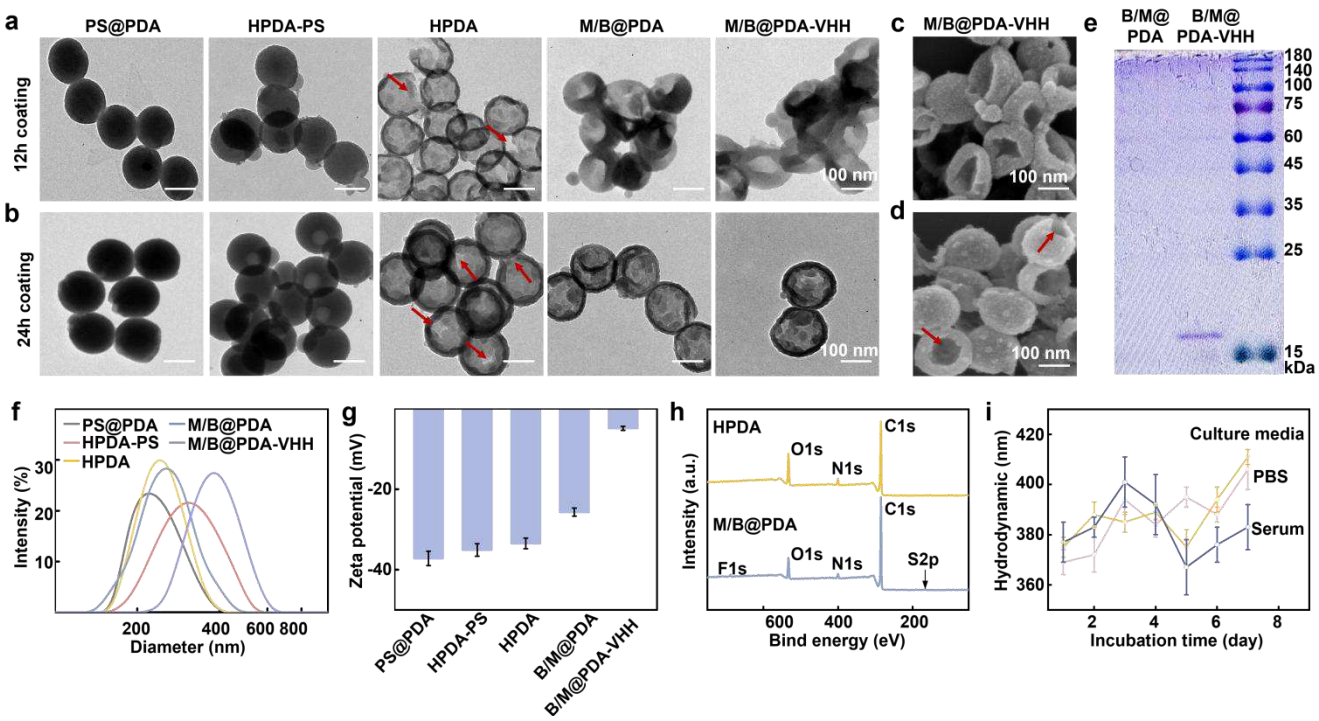


Fig. 1. Characterization of M/B@PDA-VHH NPs. (a) TEM images of PS@PDA, HPDA-PS, HPDA, M/B@PDA and M/B@PDA-VHH NPs under PDA coating for 12 and (b) 24 h. (c) SEM images of M/B@PDA-VHH NPs under 12 and (d) 24 h coating. (e) SDS-PAGE of VHH bound to M/B@PDA and M/B@PDA-VHH NPs. (f) Hydrodynamic diameters and (g) Zeta potential of PS@PDA, HPDA-PS, HPDA, M/B@PDA and M/B@PDA-VHH NPs (n = 3). (h) XPS spectra of HPDA and M/B@PDA-VHH NPs (i) Change in hydrodynamic diameter of M/B@PDA-VHH NPs after incubation with media, PBS, and serum for 7 days(n=3). Data are expressed as mean ± standard deviation (SD).

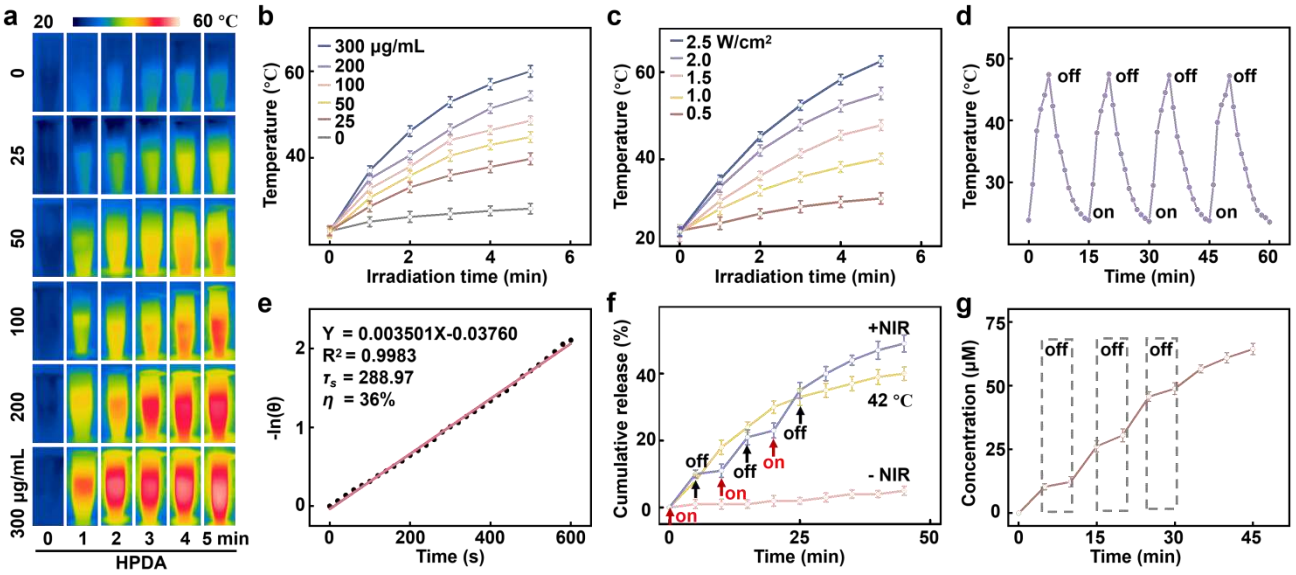


Fig. 2. In vitro photothermal properties and drug release. (a) Thermal imaging images of M/B@PDA-VHH NPs at various concentrations and treatment was performed with NIR(808 nm,1.5 W/cm²,5 min)(n=3). (b) M/B@PDA-VHH NPs at various concentrations and (c) 808 nm laser power (0-2.5 W/cm^2) for 5 min (n=3). (d) Photothermal stability graph of M/B@PDA-VHH suspensions under NIR irradiation for 4 cycles. (e) The relationship between the negative natural logarithm of temperature and cooling time in the cooling stage. (f) The M216 release from M/B@PDA-VHH NPs after intermittent NIR irradiation for 5 min with 3 cycles, using those without NIR irradiation and heating to 42° C as control (n = 3). (g) NO generation after intermittent NIR irradiation for 5 min with 3 cycles (n = 3).

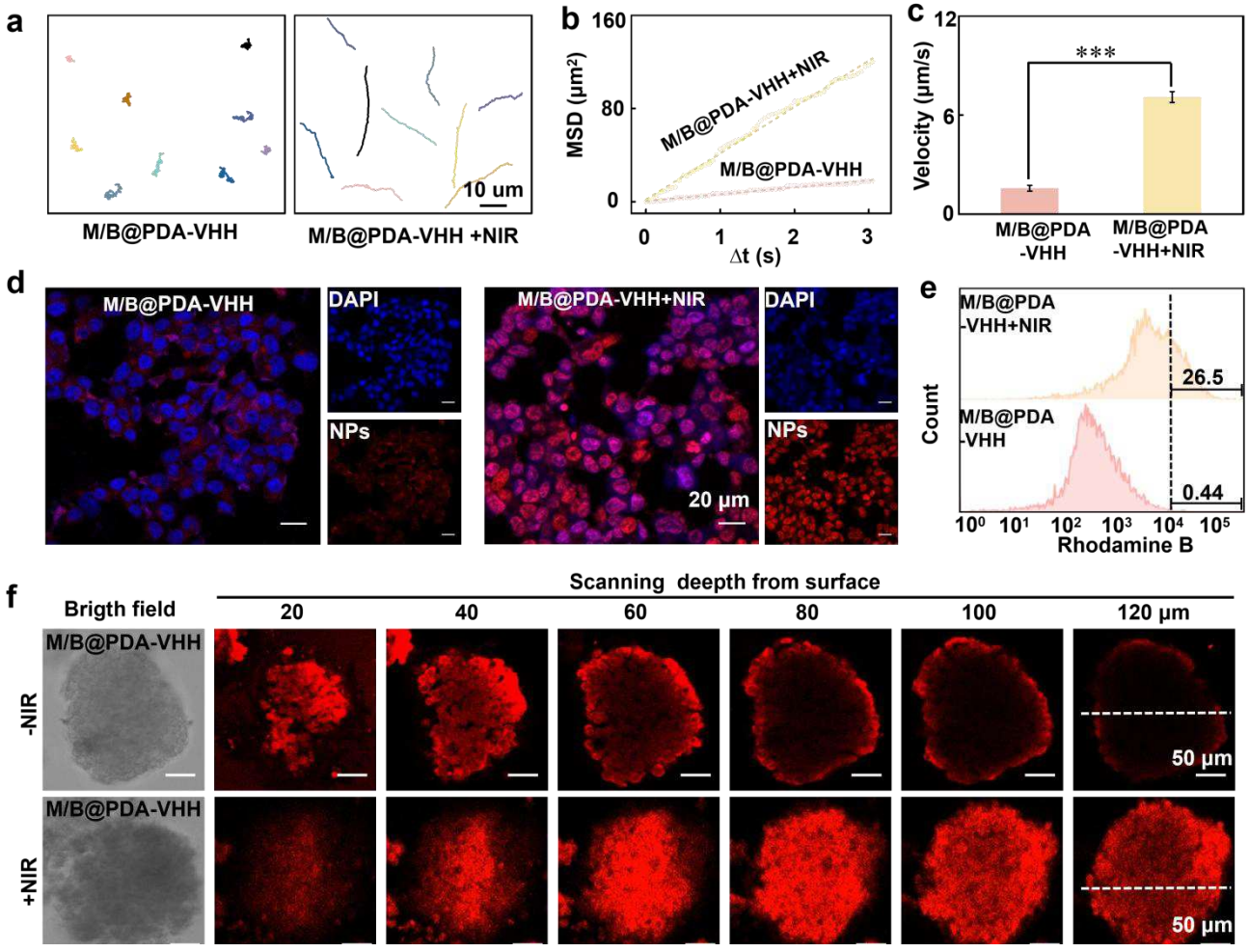


Fig.3. In vitro motion profiles and penetration ability. (a) Tracking trajectories, (b) average MSD values and (c) motion velocities of M/B@PDA-VHH NPs with or without NIR irradiation treatment(n=20). (d) CLSM images and (e) FCM analysis of 22RV1 cells collected from the lower chamber of the transwell. (f) CLSM images of 3D 22RV1 spheroids acquired through layer-by-layer scanning at step size of 20 μm. The spheroids were treated with Rhodamine B-labeled M/B@PDA-VHH NPs with or without NIR irradiation treatment for 5 min. Data are presented as mean ± SD.***$p < 0.001$.

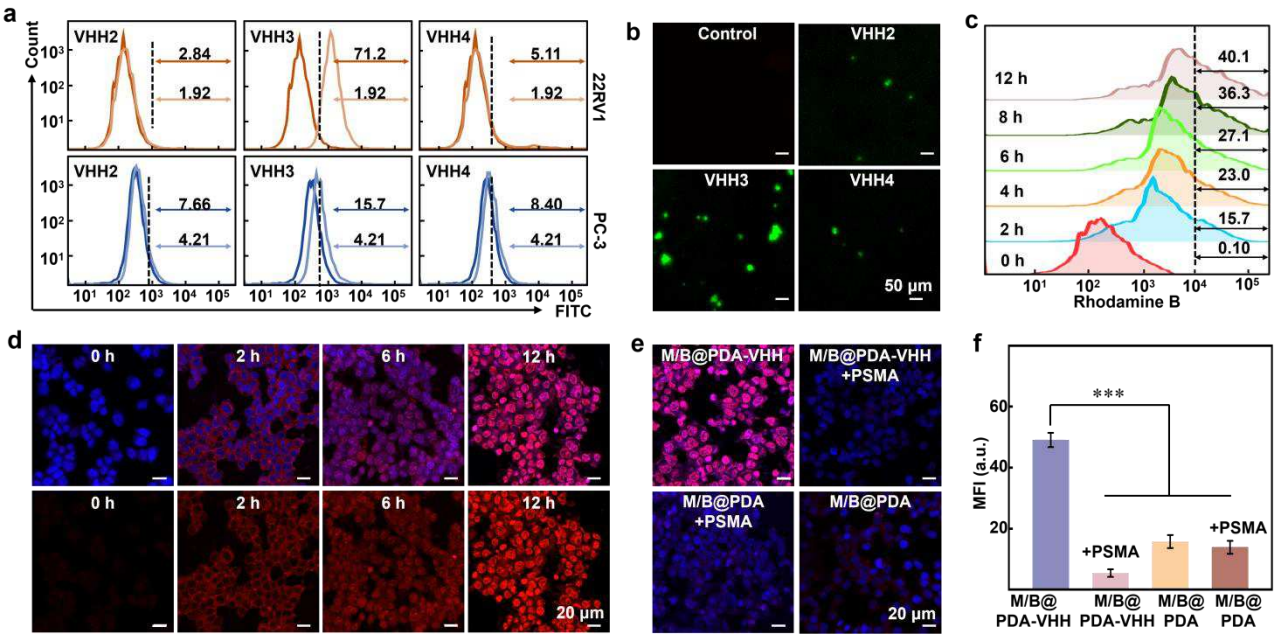


Fig. 4. Cellular internalization of M/B@PDA-VHH NPs. (a) FCM analysis of FITC-labeled nanobodies (VHH2, VHH3, and VHH4) binding to 22RV1 (PSMA positive) and PC3 cells (PSMA negative). (b) Fluorescence images of VHH2, VHH3, and VHH4 NPs binding to Alexa Fluor 488-labeled PSMA antigen in vitro. (c) FCM analysis and (d) CLSM images of PSMA- expressing 22RV1 following exposure to M/B@PDA-VHH for different time. (e) CLSM images and (f) corresponding fluorescence intensity of 22RV1 cell after incubation with M/B@PDA and M/B@PDA-VHH NPs. NPs were pre-incubated with or without exogenous PSMA antigen(n=3). Data are presented as mean ± SD. ***$p < 0.001$.

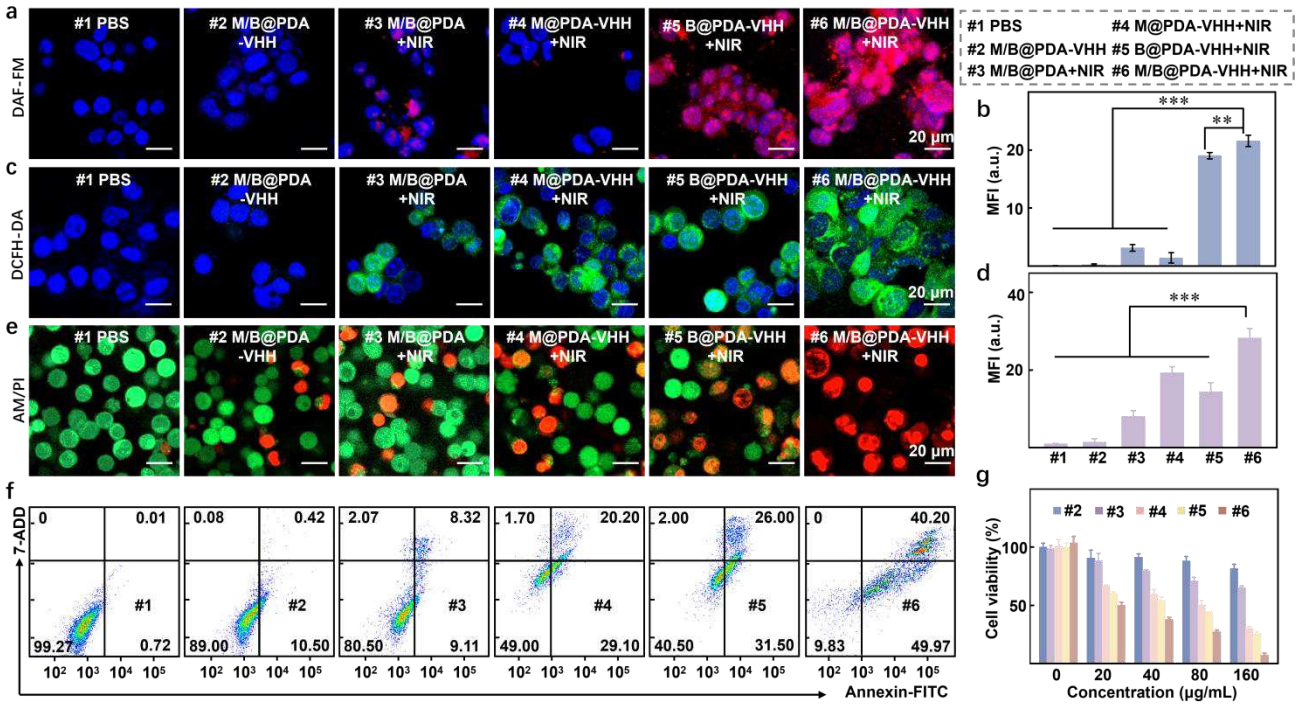


Fig. 5. In vitro antitumor effect of M/B@PDA-VHH NPs. (a) CLSM images and (b) corresponding fluorescence intensity of DAF-FM DA stained after incubation with PBS, M/B@PDA-VHH, M/B@PDA+NIR, M@PDA-VHH+NIR, B@PDA-VHH+NIR and M/B@PDA-VHH+NIR (n=3). (c) CLSM images and (d) corresponding fluorescence intensity of DCFH-DA in 22RV1 cells under different treatment conditions (n=3). (e) Calcein-AM/PI staining by CLSM images and (f) apoptosis apoptosis analysis of 22RV1 cells following various treatments. (g) Cell viability of 22RV1 after different treatment conditions (n=3).**$p < 0.01$, ***$p < 0.001$.

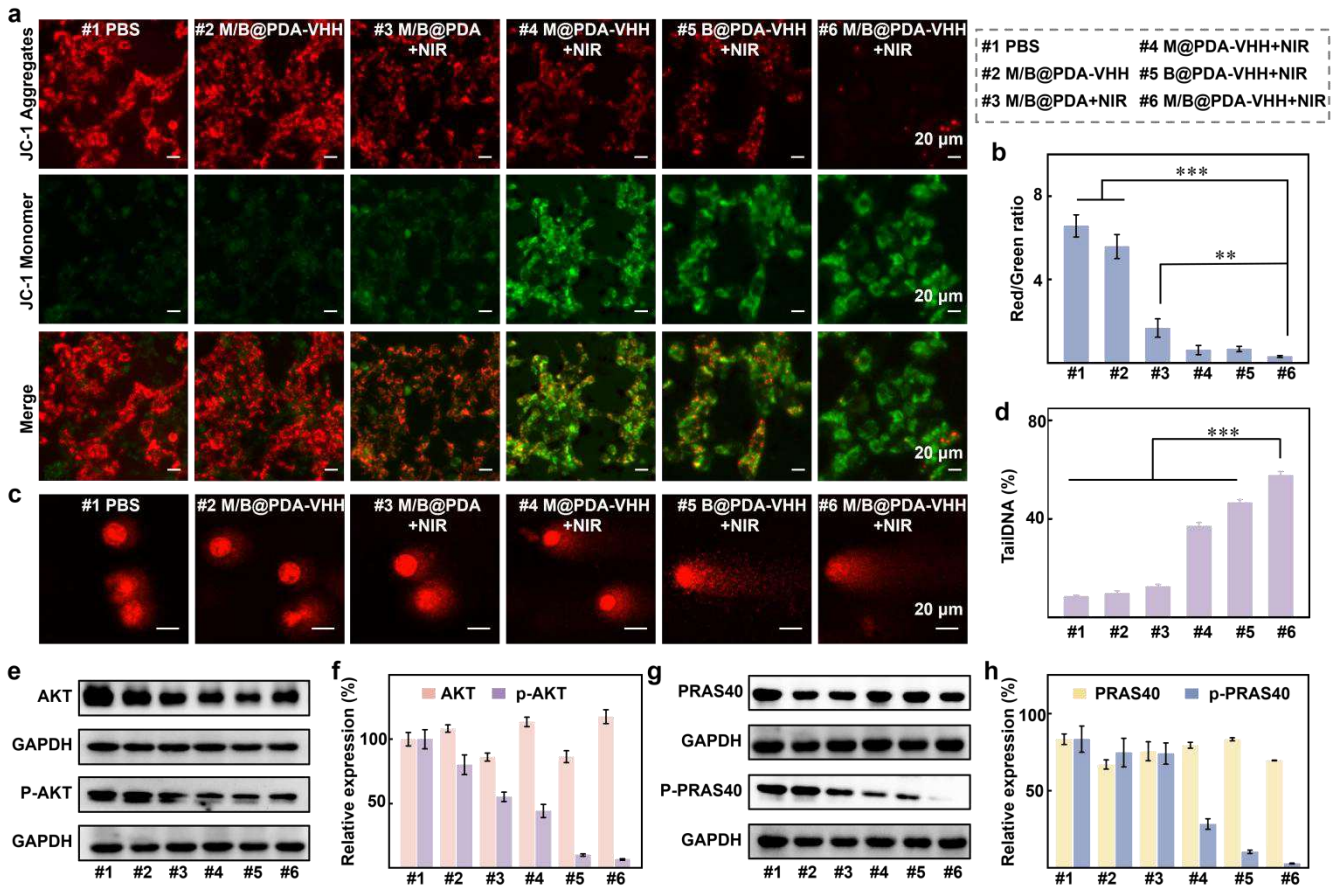


Fig. 6. In vitro anti-PCa mechanism investigation of M/B@PDA-VHH NPs. (a) CLSM images and (b) fluorescence quantification analysis of JC-1 staining 22RV1 cells after treatments with PBS, M/B@PDA-VHH, M/B@PDA+NIR, M@PDA-VHH+NIR, B@PDA-VHH+NIR and M/B@PDA-VHH+NIR (n=3). (c) DNA damage evaluation via comet assay and (d) corresponding quantitative analysis of tailDNA% after different treatment (n=3). (e) Western blot images of AKT and p-AKT proteins, and (f) corresponding quantitative analysis (n=3). (g)Western blot images of PRAS40 and p-PRAS40 proteins, and (h) corresponding quantitative analysis (n=3). $^{**}p < 0.01$, $^{***}p < 0.001$.

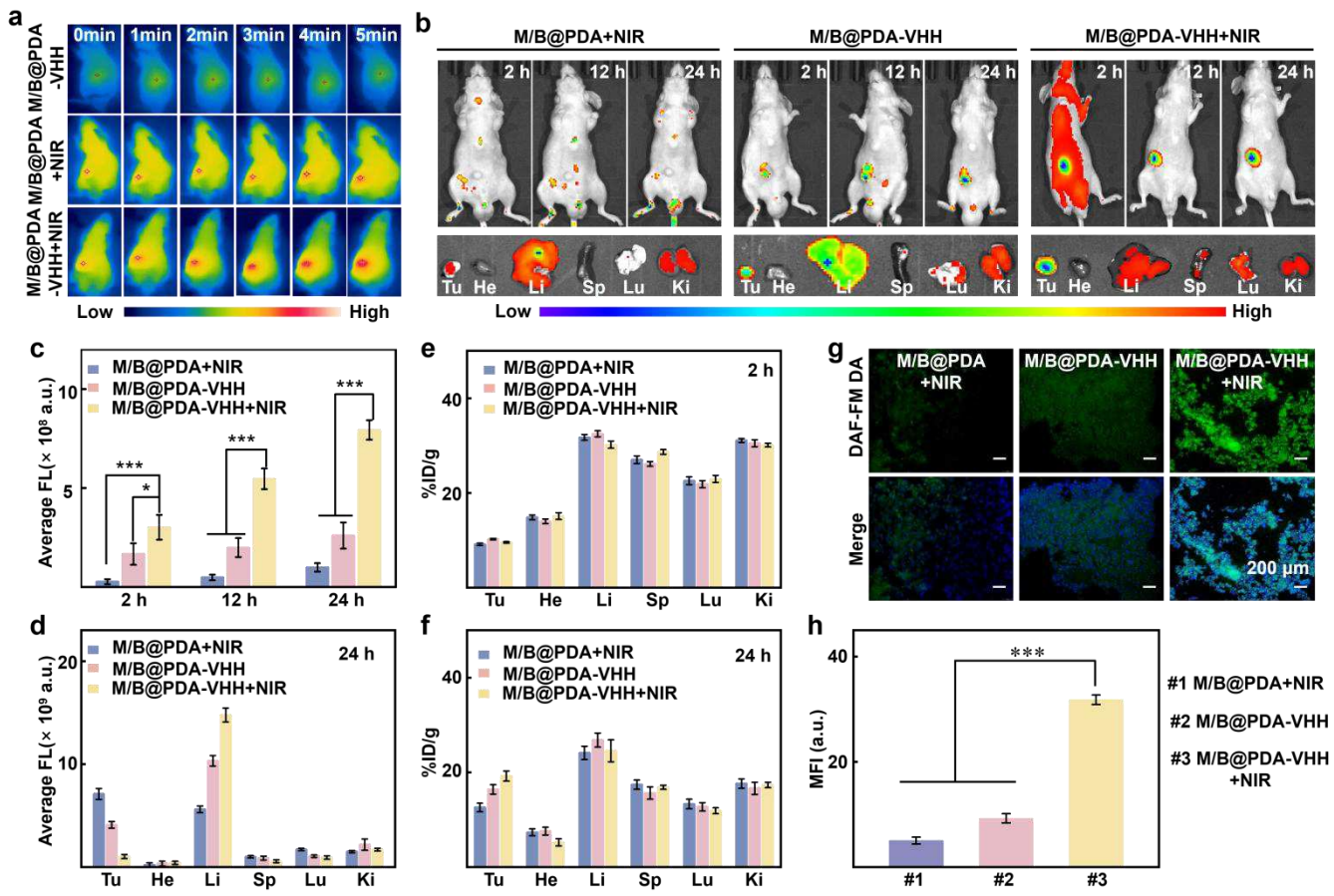


Fig. 7. In vivo target and tissue distribution of M/B@PDA-VHH NPs. (a) Thermographic images of mice with tumors after treatment with M/B@PDA or M/B@PDA-VHH NPs for 24 h, and then NIR irradiation for 5 min. (b) IVIS imaging of Cy5-labeled NPs biodistribution in tissues and major organs at different time points. (c) Semi-quantitative fluorescence analysis of Cy5-labeled NPs in subcutaneous 22RV1 tumors and (d) major organs at various time points (n = 3). (e) Biodistributions in the tumor and major organs after administration of M/B@PDA+NIR, M/B@PDA-VHH,and M/B@PDA-VHH+NIR at 2 and (f) 24 h (n = 3). (g) CLSM images and (h) corresponding fluorescence intensity of tumor sections from DAF-FM DA-administered mice after 24 h of different treatments (n=3). *$p < 0.05$, ***$p < 0.001$.

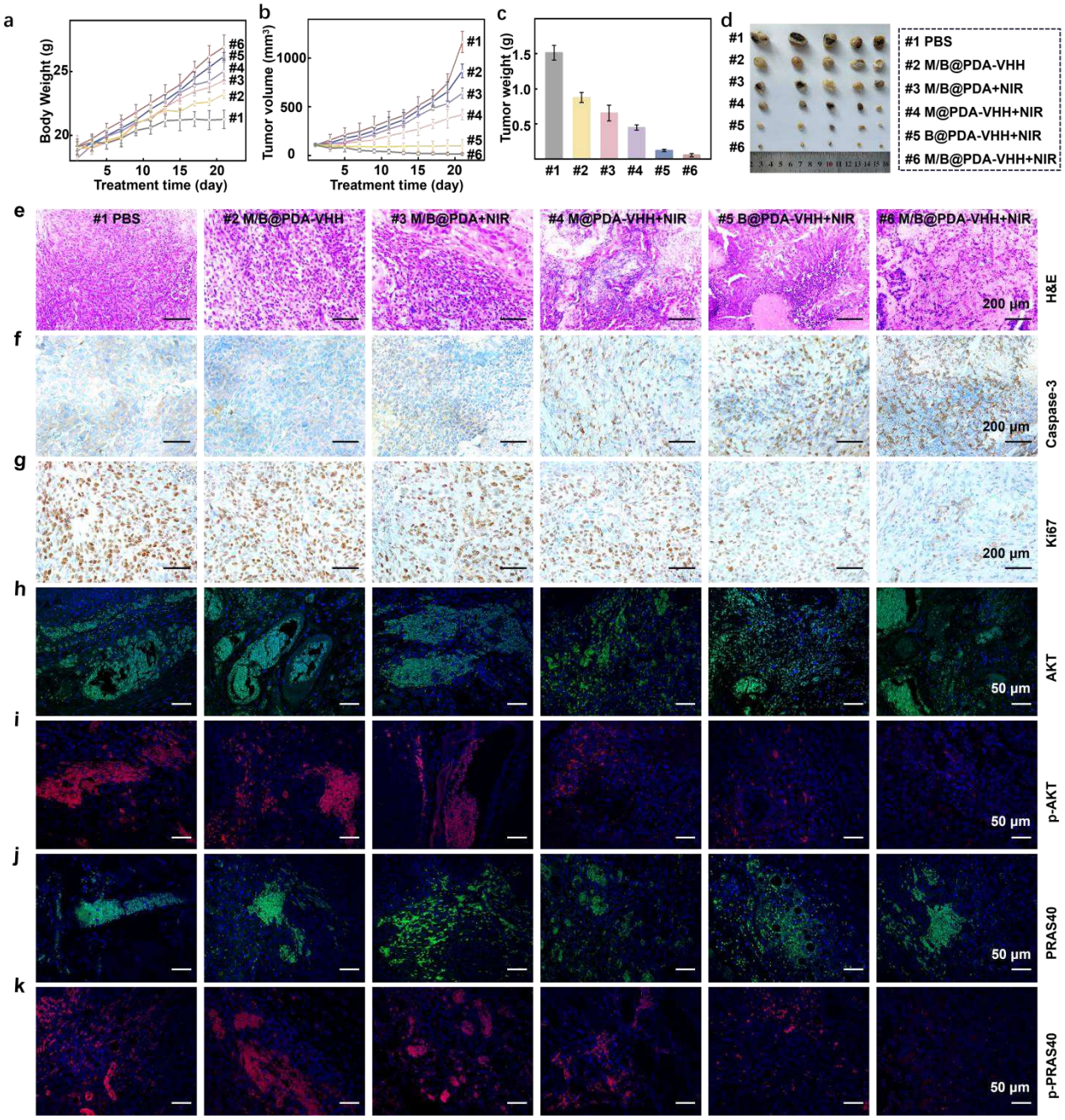


Fig. 8. In vivo anti-PCa efficacy of M/B@PDA-VHH NPs. (a) Tumor growth curves, (b) body weight, (d) tumor weight and (d) images of 22RV1 bearing mice after PBS, M/B@PDA-VHH, M/B@PDA+NIR, M@PDA-VHH+NIR, B@PDA-VHH+NIR and M/B@PDA-VHH+NIR treatment on day 21 (n=6). (e) H&E staining, (f) caspase-3 and Ki-67 (g) protein expression by IHC in tumors after 21-day treatments (n=6). (h) Immunofluorescence of AKT, (i) p-AKT, (j) PRAS40 and (k) p-PRAS40 of tumor section after different treatment.

Supplementary Files

This is a list of supplementary files associated with this preprint. Click to download.

- SupportingInformation.docx